Tailoring microstructure and mechanical properties of sintered Cu nanoparticles

Du, Leiming; Schaffar, Gerald; Jiao, Weiping; Liu, Kai; Poelma, René H.; Fan, Jiajie; van Driel, Willem D.; Fan, Xuejun; Zhang, Guoqi; More Authors

DOI
10.1016/j.actamat.2025.121501

Publication date
2025

Document Version
Final published version

Published in
Acta Materialia

Acta Materialia 300 (2025) 121501

Contents lists available at ScienceDirect

Acta Materialia

journal homepage: www.elsevier.com/locate/actamat

Full length article

Tailoring microstructure and mechanical properties of sintered Cu nanoparticles

Leiming Du [a], Gerald Schaffar [b], Weiping Jiao [a], Kai Liu [c], René H. Poelma [a,*], Verena Maier-Kiener [b,*], Jiajie Fan [d,*], Daniel Kiener [b], Willem D. van Driel [a], Xuejun Fan [e], Guoqi Zhang [a]

[a] Department of Microelectronics, Delft University of Technology, Mekelweg 4, Delft, 2628 CD, The Netherlands
[b] Department Materials Science, Montanuniversitat Leoben, Roseggerstrasse 12, Leoben, 8700, Austria
[c] Department of Materials Science and Engineering, Delft University of Technology, Mekelweg 2, Delft, 2628 CD, The Netherlands
[d] Shanghai Engineering Technology Research Center for SiC Power Device, Academy for Engineering & Technology, Fudan University, 220 Handan Rd., Shanghai, 200433, China
[e] Department of Mechanical Engineering, Lamar University, P.O. Box 10028, Beaumont, TX 77710, USA

ARTICLE INFO

Keywords:
Cu nanoparticles
Sintering pressure
Micro-pillar compression
Transmission Kikuchi diffraction
Molecular dynamics

ABSTRACT

This study investigates the microstructure evolution and mechanical behavior of bimodal-sized sintered copper (Cu) nanoparticles (NPs) under varying sintering pressures. Micro-pillar compression tests reveal a transition from collapse-dominated to compaction-driven deformation as sintering pressure increases. Transmission electron microscopy (TEM) and transmission Kikuchi diffraction (TKD) analyses identify a two-stage deformation mechanism—initial pore compaction followed by intragranular slip—fundamentally distinct from bulk Cu. Molecular dynamics (MD) simulations further reveal that large particles promote dislocation-mediated plasticity by accommodating intragranular slip, while small particles enhance load transfer through localized shear-compaction, together enabling uniform strain distribution and supporting the experimentally observed strain accommodation. The resulting microstructure achieves a combination of high yield strength (up to 320 MPa) and low elastic modulus (20 GPa), offering a compliant yet robust response. These findings elucidate a unique processing–structure–property relationship and provide a rational basis for designing porous metal interconnects capable of withstanding thermomechanical stresses in advanced electronic packaging.

1. Introduction

Pressure-assisted sintering enables the rapid densification of metallic nanoparticles (NPs) at relatively low temperatures, significantly reducing processing time compared to conventional pressureless sintering [1,2]. Copper (Cu) NPs consolidated via this method exhibit superior electrical, thermal, and mechanical properties [3,4], making them highly attractive for high-throughput and reliable electronic packaging. However, the resulting microstructure—particularly porosity and neck formation—is highly sensitive to sintering pressure, directly influencing mechanical performance [5,6]. While previous studies have extensively investigated the relationship between sintering parameters, microstructure and mechanical behavior, the focus has largely remained at the macroscale [7–14]. The microscale mechanical response, especially the roles of porosity and sintered necks, remains inadequately understood. Therefore, establishing a clear correlation among sintering pressure, microstructural features and mechanical properties is critical for optimizing the reliability of sintered Cu NPs in advanced engineering applications.

Previous studies have explored the microscale mechanical behavior of sintered NPs using in-situ scanning electron microscopy (SEM) tensile tests [15–17] and micro-cantilever bending tests [17–20], however, investigations focusing on micro-pillar compression tests, particularly for sintered Cu NPs, remain limited. Micro-pillar compression test has emerged as a powerful technique for characterizing the microscale mechanical properties of materials [21–30]. Its ability to isolate small, representative material volumes reduces geometric and size-related artifacts, enabling precise analysis of key features such as porosity and sintered necks. This makes it particularly effective for studying localized deformation mechanisms that govern the mechanical response of sintered NPs [26,27]. For instance, Chen et al. [26] demonstrated

* Corresponding authors.
E-mail addresses: L.Du@tudelft.nl (L. Du), rene.poelma@nexperia.com (R.H. Poelma), verena.maier-kiener@unileoben.ac.at (V. Maier-Kiener), jiajie_fan@fudan.edu.cn (J. Fan).

https://doi.org/10.1016/j.actamat.2025.121501
Received 3 February 2025; Received in revised form 29 August 2025; Accepted 29 August 2025
Available online 6 September 2025

through micro-pillar compression tests that the mechanical performance of sintered silver (Ag) particles is strongly influenced by porosity and necking growth, with Ag flakes achieving superior bonding strength above 30 MPa due to enhanced neck formation from self-generated NPs. Inspired by such findings, this study employs micro-pillar compression tests to systematically investigate the influence of sintering pressure on the mechanical properties of sintered Cu NPs.

Investigating microstructure evolution during sintering is crucial for optimizing material performance, particularly mechanical properties. However, experimental methods face limitations in capturing the dynamic evolution of sintered Cu NPs, prompting the development of various computational models, including Molecular Dynamics (MD) [31,32], phase-field modeling [33–36], Monte Carlo (MC) simulations [37–39], finite element methods (FEM) [40–42], and the Discrete Element Method (DEM) [34,43–46]. Among these, the phase-field approach offers a key advantage by naturally simulating the evolution of complex microstructures without explicitly tracking interfaces or imposing predefined assumptions. Notably, Dzepina et al. [35] introduced a phase-field sintering model incorporating an efficient contact mechanics algorithm, enabling the simulation of pressure-assisted sintering. DEM, on the other hand, excels in modeling large-scale particle packing and neck formation [45], providing insights into the structural development of sintered materials. Due to the computational challenges associated with representing particle shapes and capturing sintering physics, most approaches—except for DEM—are typically restricted to a limited number of particles, often within a 2D framework. MC simulations, in contrast, have demonstrated the ability to model relatively large particle ensembles, effectively capturing the microstructure evolution and kinetic processes of solid-state sintering [39]. However, a key drawback of the MC method is the lack of direct physical interpretation for model parameters and time steps (Monte Carlo steps). Additionally, MC models are generally constrained to free sintering [47], limiting their applicability to pressure-assisted sintering scenarios.

MD simulations are a powerful tool for investigating atomic-scale sintering mechanisms, such as neck formation and atomic diffusion [48–53]. Although their limited timescales lead to an underestimation of diffusion-driven densification—particularly surface and bulk diffusion—MD provides precise control over sintering conditions, enabling systematic analysis of the effects of pressure on mass transport, dislocation generation, and sintered neck stability. Compared to other computational approaches, MD excels in capturing real-time atomic diffusion and neck evolution during sintering. For instance, Wang et al. [31] demonstrated the temperature-dependent sintering behavior of Cu NPs, showing that enhanced surface diffusion and atomic motion at sintering necks facilitate bonding under elevated pressures. Moreover, MD allows direct observation of dislocation activity and stacking fault accumulation during both sintering and deformation, providing critical insights into localized plastic deformation. Given these advantages, MD simulations were employed in this study to examine the sintering dynamics and mechanical deformation of sintered Cu NPs.

The aim of this study is to investigate the influence of sintering pressure on the microstructure evolution and mechanical properties of sintered Cu NPs. To achieve this, sintered Cu NPs were fabricated with increasing sintering pressure from 0 to 30 MPa, and their mechanical behavior was systematically examined through micro-pillar compression tests. Post-deformation microstructural analysis was performed using SEM, transmission electron microscopy (TEM) and transmission Kikuchi diffraction (TKD) analyses to reveal the deformation mechanisms and crystallographic orientations. Additionally, MD simulations were employed to reveal atomic-scale sintering dynamics and mechanical deformation. By integrating experimental and computational approaches, this study provides comprehensive insights into sintering and deformation mechanisms of sintered Cu NPs.

2. Experimental and simulation method

2.1. Sample preparation

To fabricate sintered Cu samples, a layer of Cu paste was initially printed onto an Active Metal Brazing (AMB) substrate with dimensions of 3 mm × 3 mm and a thickness of 200 μm. The AMB substrate consists of a silicon nitride (Si_3N_4) ceramic core bonded to finished Cu layers. The sintering process was carried out under a nitrogen atmosphere at 250 °C for 5 min using a sintering system (Sinterstar, Boschman Technologies BV), with simultaneous application of external pressure to enhance densification of the Cu NPs (Fig. 1a). After sintering, the applied aluminum (Al) film was carefully removed, leaving a consolidated Cu layer firmly adhered to the substrate (Fig. 1b). Subsequently, the sintered Cu layer was sectioned from the AMB substrate to isolate specific regions for further mechanical characterization (Fig. 1c).

Micro-pillar fabrication was performed using focused ion beam (FIB) milling (Fig. 1d) with a dual-beam FEI Helios G4 CX FIB-SEM system. This technique enabled the precise removal of material surrounding the target region, producing cylindrical micro-pillars with well-defined geometries. The fabricated micro-pillars exhibited a diameter of approximately 6 μm and a height of 20 μm, as confirmed by the SEM image in Fig. 1e. This gives an aspect ratio (height to diameter) of around 3:1, ensuring mechanical stability during compression tests [26].

2.2. Micro-pillar compression tests

The micro-pillar compression tests were conducted using an InSEM HT System (KLA Corporation, Milpitas, CA, USA), equipped with an InForce 50 actuator capable of applying a maximum load of 50 mN [54]. A flat punch tip, acquired from Synton-MDP (Nidau, Switzerland), was employed for precise load application. The boron carbide tip used in the tests has a Young's modulus of 461 GPa and a Poisson's ratio of 0.21. To ensure reproducibility and statistical significance, five micro-pillars were tested under each experimental condition. The tests were performed in displacement control mode, with continuous load–displacement data acquisition to monitor the mechanical response of the micro-pillars. Prior to testing, samples were meticulously aligned to ensure axial loading and minimize bending effects. Additionally, a pre-conditioning load was applied to establish consistent contact and eliminate surface irregularities. Post-compression, the deformation behavior of the sintered Cu micro-pillars was analyzed, focusing on key mechanical properties such as yield strength, strain hardening and failure mechanisms.

2.3. SEM and TEM characterization

To investigate the internal microstructure of the sintered Cu NPs, a focused ion beam scanning electron microscopy (FIB-SEM) three-dimensional (3D) reconstruction technique was employed. This method enables high-resolution imaging of subsurface features through a sequential milling and imaging process. The procedure began with the identification of the region of interest (ROI), as highlighted in Fig. 2a, where the imaging area was demarcated. To ensure precise alignment and accurate relocation throughout the milling process, a fiducial marker was fabricated on the sample surface (Fig. 2b). Material removal was performed systematically using the FIB along the designated milling direction, and each newly exposed cross-sectional surface was imaged using SEM. The resulting two-dimensional (2D) SEM images were sequentially collected and stacked to generate a high-resolution 3D reconstruction of the microstructure (Fig. 2c) by using a commercial software Avizo. Despite the protective deposition of a Pt layer over the ROI prior to milling, minor damage to the Pt layer was observed due to the ion beam, as illustrated in Fig. 2d. This highlights a common challenge in FIB-based sample preparation, particularly for sensitive

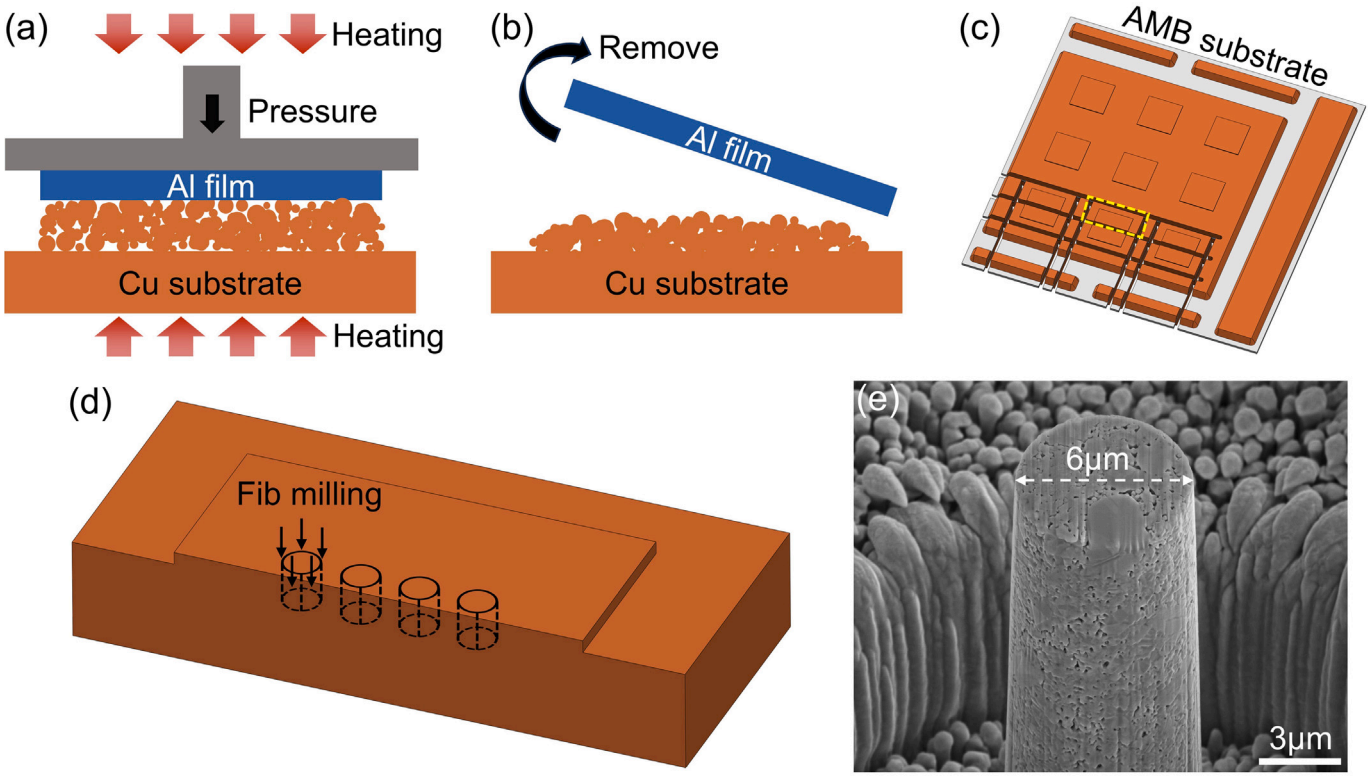

Fig. 1. (a) Diagram of sintering process (250 °C, 5 min); (b) Al film removal; (c) sintered Cu pattern on AMB substrate; (d) FIB milling process; (e) a typical SEM image of the micro-pillar.

surface layers, but did not significantly affect the overall integrity of the 3D dataset.

Following 3D reconstruction, compression-tested micro-pillars were analyzed to investigate the failure mechanisms. The post-compression morphology was examined using SEM, enabling the identification and comparison of typical failure modes across samples prepared under different sintering pressures. To further elucidate the deformation mechanisms, transmission electron microscopy (TEM, Cs-corrected Titan) was employed for a detailed microstructure analysis of the deformed micro-pillars at the nanoscale. In this study, three TEM samples were fabricated on 20 MPa sintered Cu nanoparticle (NP) micro-pillars (Fig. S1). Moreover, TKD was employed to characterize the crystallographic orientation of sintered Cu NP micro-pillars after deformation. Although electron backscatter diffraction (EBSD) is widely used in micromechanical studies [55,56], its spatial resolution (50–100 nm) is insufficient for resolving the submicron grain structure and porosity typical of sintered Cu NPs. In contrast, TKD offers spatial resolutions below 10 nm [57, 58], enabling statistically meaningful microstructural characterization critical for understanding microscale deformation mechanisms.

2.4. Molecular dynamics simulation

The sintering and mechanical behavior of bimodal Cu NP models were investigated using MD simulations with the Large-scale Atomic/Molecular Massively Parallel Simulator (LAMMPS) [59]. The atomic configurations, dislocations and local crystallographic environments during sintering and deformation were visualized and analyzed using the Open Visualization Tool (OVITO) [60]. The Cu–Cu atomic interactions were modeled using the Embedded Atom Method (EAM) potential proposed by Mishin et al. [61], which has been widely validated for simulating diffusion, grain boundary migration and mechanical responses in Cu systems. A 3D bimodal particle model was constructed within a simulation box measuring 800 × 800 × 100 $Å^3$, as shown in Fig. 3. Large cylindrical particles (diameter: 25 nm; height: 10 nm along the z-axis) were initially positioned in the simulation domain, and 1500 smaller spherical particles (average diameter: 2.5 nm) were randomly introduced to fill the voids around the cylinders, ensuring a high packing density of approximately 55%. The final model consisted of 3.1 million atoms. The sintering process was simulated in three stages. First, the system temperature was gradually increased to 523 K using a Nosé–Hoover thermostat to facilitate NP diffusion and sintering. Next, uniaxial strains of 30%, 40% and 50% were applied sequentially along the X- and Y-axes to simulate pressure-assisted sintering and replicate the height reduction observed in experiments. During this step, lateral pressures in the non-loading directions were maintained at zero, and a strain rate of 1×10^9 s^{-1} was employed. The system was then equilibrated at 523 K for 100 ps to relax residual stresses from the high strain rate, resulting in a sintered model.

To evaluate the mechanical response of the sintered Cu NPs, tensile and compression simulations were performed along the X- and Y-directions (the long axes of the model), based on the previously sintered configurations. This resulted in 12 distinct stress–strain curves corresponding to the sintered models under three different applied strains (30%, 40%, and 50%) and two loading directions (tensile along X and Y, compression along X and Y). Tensile and compression simulations were performed under fully periodic boundary conditions using the NPT ensemble, with the temperature maintained at 300 K. A maximum tensile strain of 30% was applied at a strain rate of 5×10^8 s^{-1}, a value consistent with prior studies [62]. Compressive strains, on the other hand, were applied up to approximately 16%, aligning with experimental results. Stresses in the non-loading directions were maintained at zero during both tensile and compressive simulations to replicate uniaxial loading conditions.

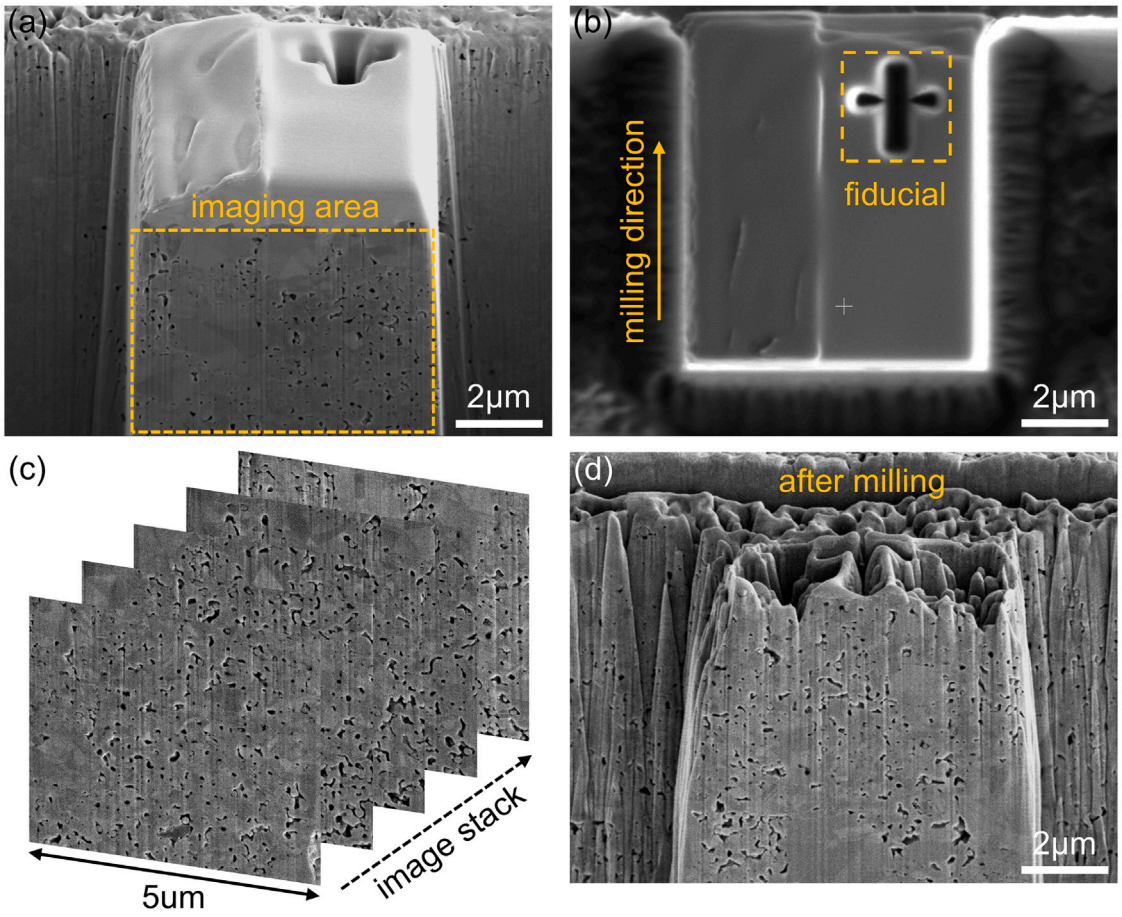

Fig. 2. FIB-SEM slice-and-view procedure: (a) Deposition of Pt layer and imaging area; (b) fiducial marking for milling; (c) stacked SEM slices; (d) reconstructed region after milling.

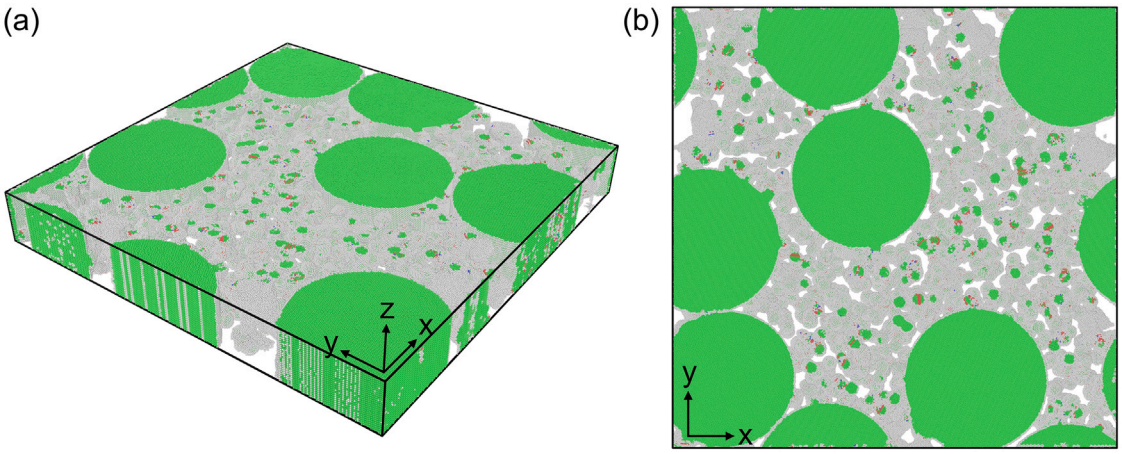

Fig. 3. Sintered Cu NPs with bimodal size distribution and periodic boundary conditions for MD simulation: (a) 3D perspective model; (b) orthogonal view of (a).

3. Results

3.1. Effect of sintering pressure on porosity

The influence of sintering pressure on the porosity and microstructure of sintered Cu NPs was investigated using a combination of 2D cross-sectional imaging and 3D FIB-SEM reconstruction. Fig. 4 presents 2D cross-sectional images of samples sintered under different pressures, providing a detailed characterization of porosity evolution and void morphology. Before sintering (Fig. 4a), the Cu NPs exhibit a significant bimodal size distribution. At 0 MPa (Fig. 4b), the Cu NPs retain their distinct morphology with clear and well-defined particle boundaries, indicating that significant sintering has not yet occurred. Increasing the pressure to 5 MPa (Fig. 4c) enhances neck growth but leads to the formation of larger, more irregular voids. This can be attributed to particle coalescence, where larger particles consume smaller ones, resulting in isolated and irregularly shaped voids. Moreover, the distribution of voids is not uniform. In some regions, void concentration is higher.

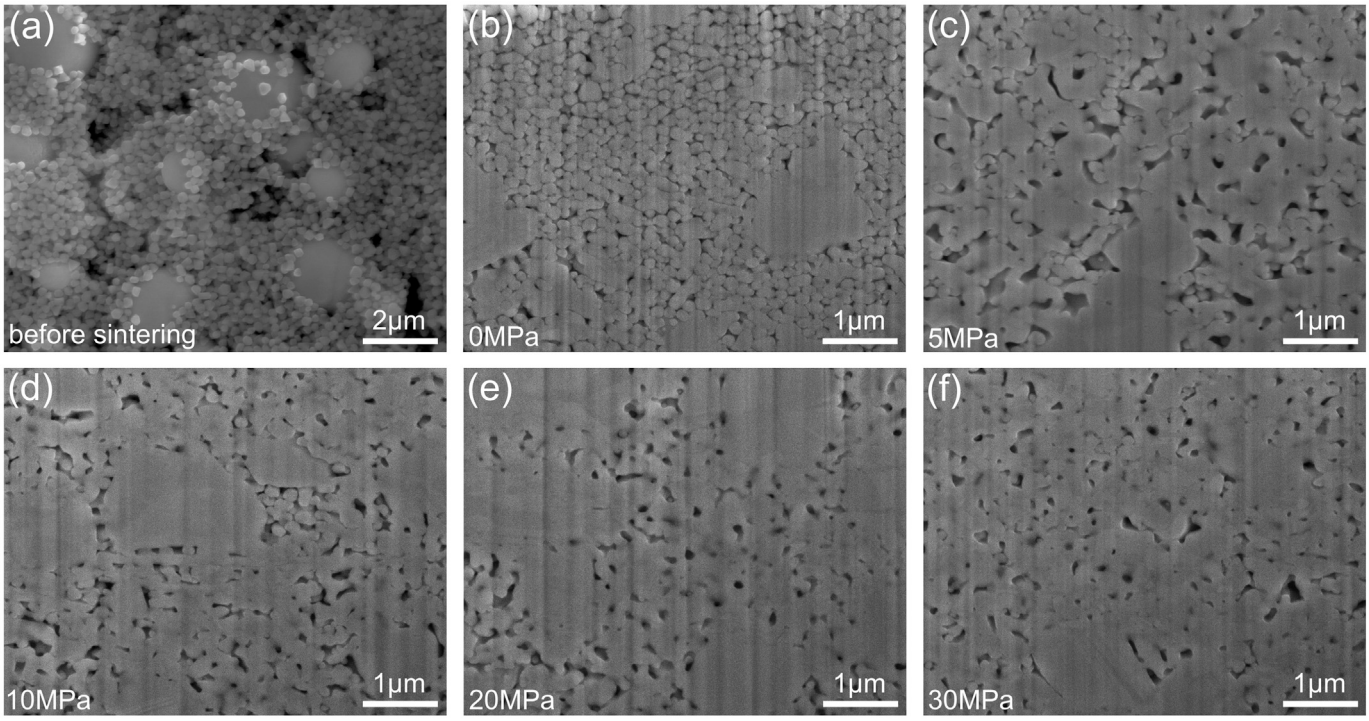

Fig. 4. Microstructure evolution of Cu NPs: (a) Before sintering; (b) sintered at 0 MPa; (c) sintered at 5 MPa; (d) sintered at 10 MPa; (e) sintered at 20 MPa; (f) sintered at 30 MPa.

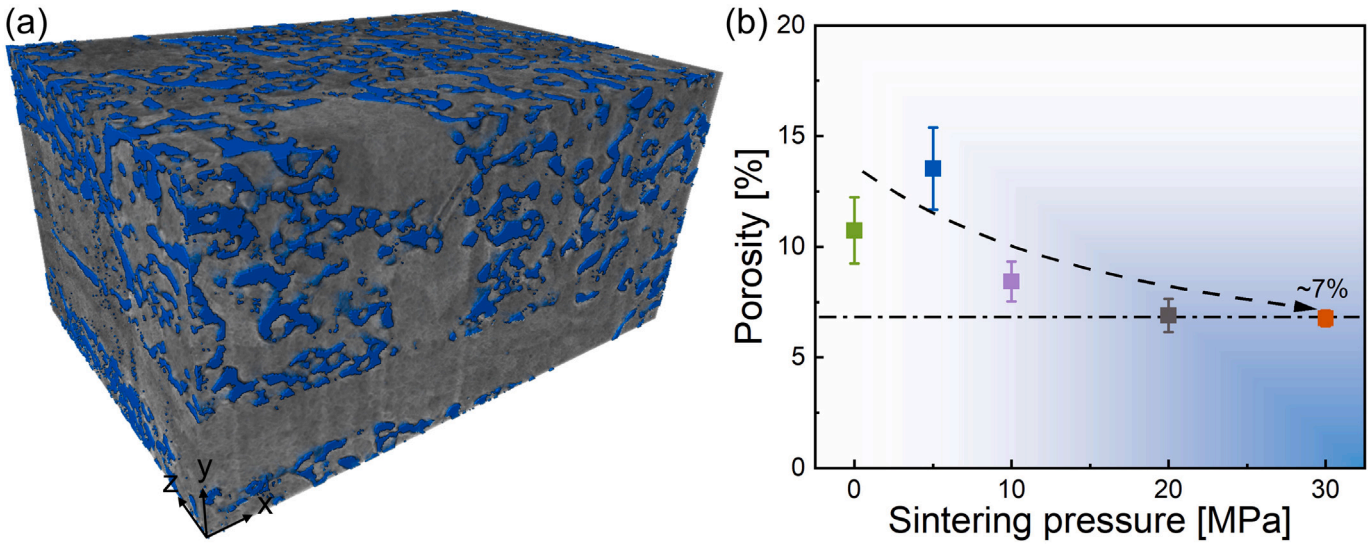

Fig. 5. (a) A 3D reconstructed structure of 5 MPa sintered sample; (b) relationship between the porosity and the sintering pressure.

At 10 MPa (Fig. 4d), the structure becomes noticeably more compact, with voids that are smaller, more rounded and less interconnected. The neck growth between particles becomes more pronounced, although isolated voids persist, indicating incomplete densification. At 20 MPa (Fig. 4e), the microstructure demonstrates significant densification with tightly packed particles and well-defined sintered necks. The voids are smaller, more uniform and exhibit a more spherical shape, suggesting that higher pressure promotes void collapse and improved particle rearrangement. Beyond 20 MPa, further increasing the pressure to 30 MPa (Fig. 4f) results in only a slight improvement in densification. The voids stabilize in size and shape, becoming uniformly distributed and more spherical.

To quantitatively measure the porosity, FIB-SEM 3D reconstruction technique were applied on the five groups of sintered samples. The 3D reconstruction results of 5 MPa sintered Cu NPs, shown in Fig. 5a, provide a clear visualization of the internal porosity of the sintered samples, with the voids represented in blue. Quantitative analysis of the 3D volume porosity extracted from the software as a function of sintering pressure is presented in Fig. 5b. It is evident that porosity decreases with increasing sintering pressure. At 0 MPa, the porosity is approximately 10%, while further increasing the pressure to 30 MPa reduces the porosity to a stable value of 7%. Two key observations arise from this trend. First, the reduction in porosity with increasing pressure is attributed to enhanced particle rearrangement, melting at contact points and sintered neck formation, which are facilitated by the applied pressure. Second, despite increasing the sintering pressure from 20 MPa to 30 MPa, the porosity stabilizes around 7%, indicating a threshold where further densification is limited by residual nanoscale voids and

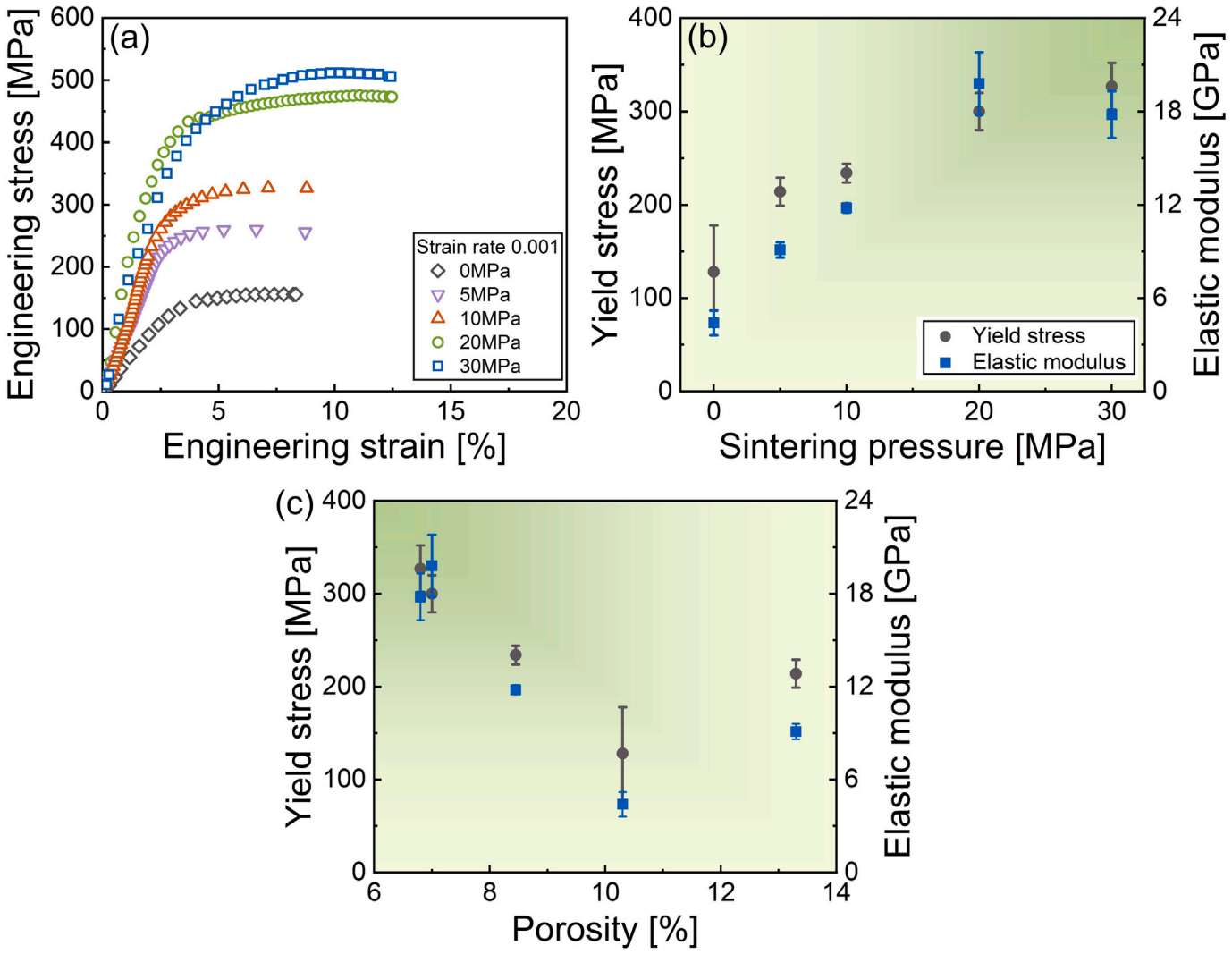

Fig. 6. Mechanical properties of sintered Cu NPs: (a) Stress–strain curves of samples sintered under pressures of 0 MPa, 5 MPa, 10 MPa, 20 MPa and 30 MPa; (b) relationship between yield stress, elastic modulus and sintering pressure; (c) relationship between yield stress, elastic modulus and porosity.

geometric constraints. Interestingly, the porosity of the sample sintered without pressure (0 MPa) is slightly lower than that of the sample sintered with pressure of 5 MPa. This anomaly can be attributed to the sintering dynamics: at 5 MPa, particle rearrangement initiates, and larger particles grow at the expense of smaller ones (Ostwald ripening [40]), leading to the formation of larger and resolvable voids. In contrast, at 0 MPa, sintering barely progresses, and the particles remain loosely packed with minimal neck growth. The resulting voids are small and difficult to resolve using FIB-SEM, which could lead to an underestimation of porosity.

In summary, the sintering pressure not only reduces porosity but also significantly influences void shape and distribution. Higher pressures transform voids from irregular and interconnected at low pressures to smaller, more spherical and evenly distributed at pressures beyond 20 MPa. Importantly, the non-uniform void distribution observed under lower pressures highlights localized sintering effects around large particles. To elucidate these mechanisms further, sintering dynamics based on MD simulations will be presented in the next section.

3.2. Stress–strain curves

The mechanical properties of sintered Cu NPs, evaluated through micro-pillar compression tests, show a strong dependence on sintering pressure and porosity (Fig. 6). The stress–strain curves for samples sintered under pressures ranging from 0 MPa to 30 MPa are presented in Fig. 6a. A clear enhancement in mechanical properties, including yield stress and elastic modulus, is observed with increasing sintering pressure. The yield strength of the sintered Cu micro-pillars was determined using the 0.2% offset yield criterion [63], a widely adopted method for defining the onset of plastic deformation in metallic materials. At 0 MPa, the stress–strain curve reveals a low yield stress of approximately 120 MPa and an ultimate strength of 150 MPa, reflecting poor interparticle bonding and high porosity that limit load transfer and lead to premature failure. Increasing the sintering pressure to 5 MPa results in an improvement in yield stress to 210 MPa and ultimate strength to 260 MPa, attributed to initial densification and neck formation between particles. At 10 MPa, further enhancement is observed, with yield stress reaching 230 MPa and ultimate strength rising to 320 MPa, indicating better particle rearrangement, reduced voids and stronger neck growth. A significant improvement occurs at 20 MPa, where the yield stress exceeds 300 MPa and the ultimate strength approaches 470 MPa. The stress–strain curve exhibits a steeper slope in the elastic region, corresponding to a notable increase in stiffness, which reflects a more optimized microstructure with fewer voids and enhanced neck formation. At 30 MPa, the yield stress increases slightly to 320 MPa, and the ultimate strength is close to 510 MPa; however, the improvement relative to 20 MPa is less pronounced.

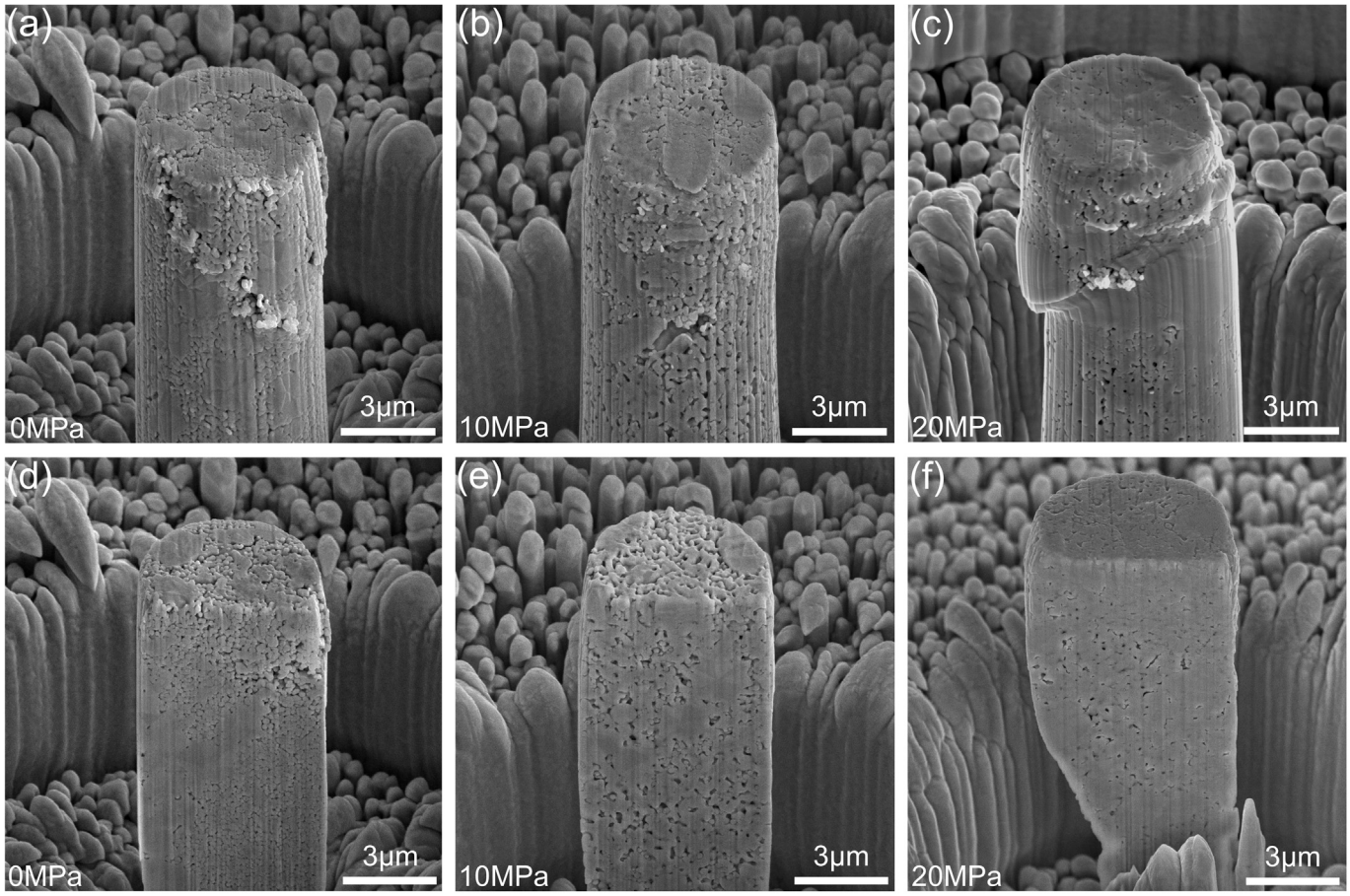

Fig. 7. Typical morphologies of micro-pillar after compression tests: (a) 0 MPa; (b) 10 MPa; (c) 20 MPa; (d) cross-section of (a); (e) cross-section of (b); (f) a typical cross-section of a 20 MPa sintered micro-pillar.

The relationship between sintering pressure, yield stress and elastic modulus is quantified in Fig. 6b. The elastic modulus increases significantly with sintering pressure, rising from 4.8 GPa at 0 MPa to 20 GPa at 20 MPa, with only a marginal gain at 30 MPa. This plateauing behavior indicates that the microstructure reaches near-optimal densification and sintered neck growth at 20 MPa, beyond which additional pressure provides diminishing returns. Fig. 6c further illustrates the correlation between mechanical properties and porosity. A clear trend emerges where decreasing porosity leads to significant improvements in both yield stress and elastic modulus. Specifically, at porosities exceeding 10%, the mechanical performance is severely limited due to insufficient neck formation and void concentration, whereas samples with porosities below 7%–8% exhibit significantly enhanced strength and stiffness.

The mechanical properties of sintered Cu NPs differ significantly from those of bulk copper in its various forms. Notably, the yield strength of sintered Cu NPs exceeds that of bulk single-crystalline Cu (40–70 MPa) [21,64–67] and bicrystalline Cu (80–120 MPa) [68–70], and is comparable to that of polycrystalline Cu (250–350 MPa) [29,71], although it remains lower than that of nanocrystalline Cu (500–800 MPa) [29,72,73]. This enhanced strength, despite the intrinsic porosity of the sintered network, highlights the effectiveness of nanoscale sintering in generating strong interparticle bonds. In contrast, the elastic modulus of sintered Cu NPs is significantly reduced (20 GPa) compared to bulk Cu (75–130 GPa across all microstructures). In electronic packaging, this combination of high yield strength and low elastic modulus provides critical advantages: the reduced stiffness accommodates thermomechanical deformation mismatches between the die, substrate, and interconnect during thermal cycling, mitigating stress-induced failure while retaining mechanical integrity.

3.3. Failure modes analysis

Fig. 7 illustrates the post-compression morphologies of sintered Cu micro-pillars under varying sintering pressures (0, 10, and 20 MPa), highlighting the evolution of deformation and failure mechanisms. At 0 MPa (Figs. 7a, d), failure is dominated by structural collapse, primarily due to weak inter-particle adhesion and insufficient neck formation. These poorly bonded particles lack the cohesion necessary to sustain shear or tensile stresses. With the application of 10 MPa (Figs. 7b, e), sintering is enhanced through the initiation of neck formation and localized particle coalescence, where larger particles partially engulf smaller ones. This improves bonding strength but still results in heterogeneous microstructures with significant unsintered regions due to limited particle rearrangement. Collapse failure is suppressed, and the failure mechanism transitions to compaction-dominated deformation. At 20 MPa (Figs. 7c, f), the pillars exhibit well-developed sintering necks and reduced porosity. The cross-sectional view reveals uniform densification and continuous bonding pathways, which alleviate stress concentrations and enable distributed plastic deformation. Clear evidence of slip traces in Fig. 7c indicates that the fully sintered structure can accommodate higher mechanical loads, marking a transition to ductile, stress-bearing behavior.

4. Discussion

4.1. Deformation mechanisms

Fig. 8 presents TEM images of the 20 MPa sintered Cu micro-pillar after compression (corresponding to Fig. 7c), revealing a heterogeneous

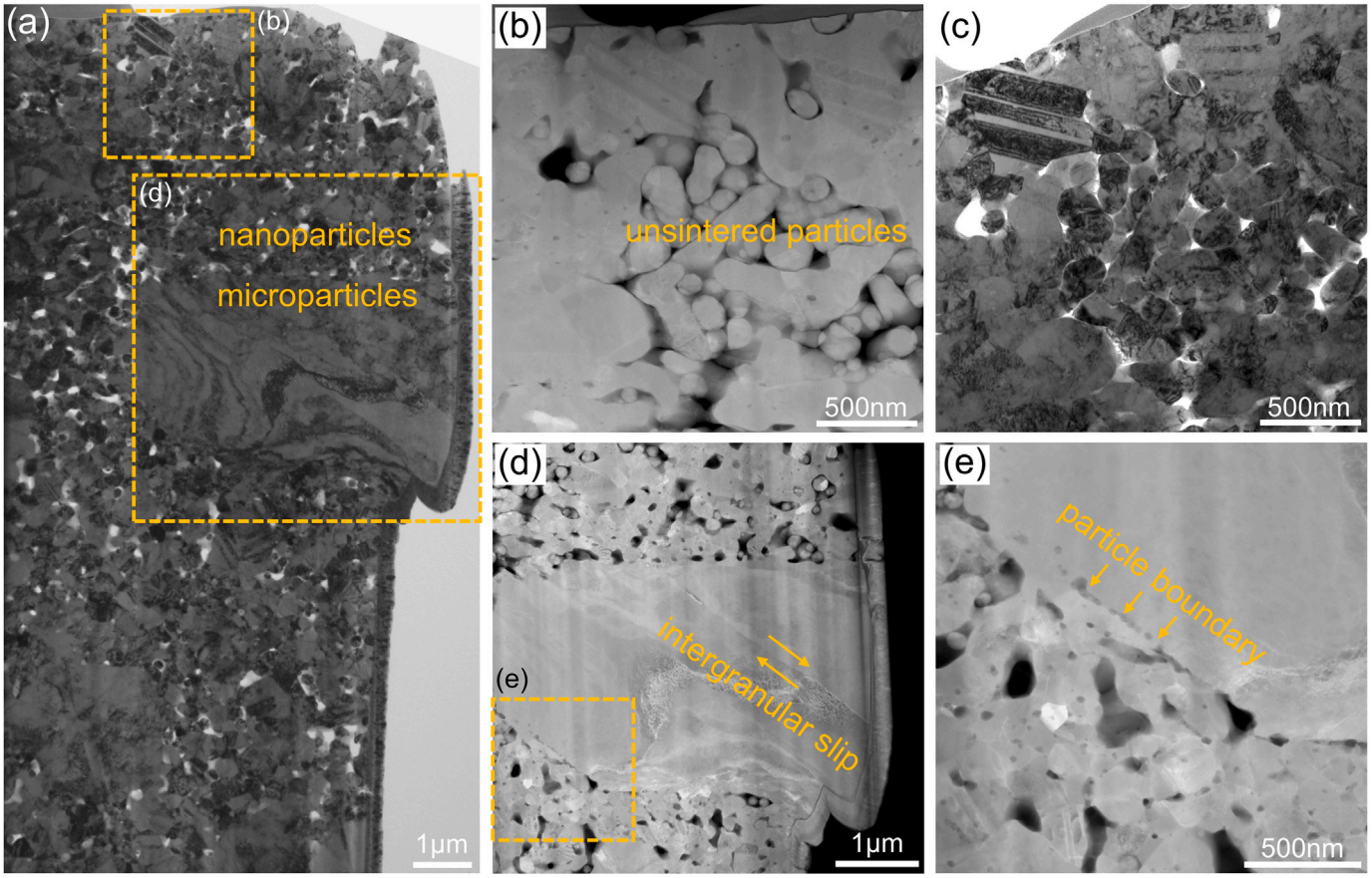

Fig. 8. TEM images of the extracted micro-pillar sintered under 20 MPa after compression test: (a) A bright-field TEM overview shows the coexistence of large and small particles; (b) scanning transmission electron microscopy (STEM) image reveals the presence of unsintered NPs; (c) bright-field image highlights dislocation structures induced by compression; (d) intergranular slip deformation observed in a large particle, indicative of plastic flow under applied stress; (e) a enlarged area marked in (d).

microstructure composed of both nano- and microparticles. As shown in Fig. 8a, the upper region and the vicinity of larger particles exhibit pronounced densification, indicative of localized compaction under compressive stress. High-magnification observations (Figs. 8b, c) reveal that initially porous regions have undergone significant pore compaction, resulting in a more continuous matrix with reduced void volume. Plastic deformation is highly localized and governed by particle size and distribution. Large particles accommodate deformation primarily through intergranular slip, as evidenced by the distinct slip bands shown in Fig. 8d, demonstrating their ability to sustain and dissipate stress. Simultaneously, smaller particles—particularly those situated at particle boundaries—undergo severe shear and compression-induced deformation, leading to localized densification (Figs. 8d, e). In addition, the oxygen distribution in the sintered Cu NPs was characterized via energy-dispersive X-ray spectroscopy (EDX) in TEM. The measured oxygen content was approximately 0.07 wt% (Fig. S2 and Table S1), which lies within the typical range for commercial-grade Cu [74]. This low level of oxidation is critical for preserving interparticle metallic bonding during sintering and promoting the formation of continuous, well-developed necks, thereby enhancing mechanical integrity.

To elucidate the localized deformation mechanisms underlying the mechanical behavior of sintered Cu NP micro-pillars, TKD analysis was performed on TEM lamellae extracted post-compression. Fig. 9a displays a representative STEM image of a micro-pillar composed predominantly of nanoparticles. The upper region undergoes severe plastic deformation, characterized by particle flattening and void compaction under compressive loading. In contrast, the lower region retains porous morphology, reflecting strain localization in the upper zone. The corresponding orientation map (Fig. 9b) confirms that the particles possess a random crystallographic orientation distribution, which inherently promotes the activation of multiple, non-collinear slip systems under compression [75]. This random texture increases the likelihood of slip transmission barriers at grain boundaries, thereby contributing to strength enhancement through grain boundary hardening [76]. The geometrically necessary dislocations (GNDs) distribution in Fig. 9c further reveals a dense dislocation network throughout the nanoparticle matrix. The widespread GNDs suggest significant plastic strain gradients and interparticle misorientation accumulation [77]. Such a dense, interconnected dislocation structure resembles dislocation forest hardening [78,79], where tangled dislocations impede further slip, enhancing strain hardening and contributing to the observed mechanical robustness. Moreover, the Schmid factor map (Fig. 9d) displays a broad spectrum of values across the microstructure, confirming that slip activity is spatially heterogeneous, consistent with the observed complex deformation behavior. Fig. 10 presents TKD analysis from a second micro-pillar containing both nano- and microparticles. The STEM image (Fig. 10a) reveals a large embedded particle within a matrix of smaller grains. Orientation mapping (Fig. 10b) shows that while smaller grains remain randomly oriented, the large particle maintains a distinct crystallographic domain. This particle likely accommodates deformation via intragranular slip [80], as supported by the high local GND density observed within and around it (Fig. 10c). The corresponding Schmid factor map (Fig. 10d) indicates that the large particle lies near a high-Schmid factor orientation, favoring slip activation.

The deformation mechanism of sintered Cu NPs exhibits fundamental differences from that of fully dense bulk copper, including single-crystalline [21,66], bicrystalline [69,70], polycrystalline [29],

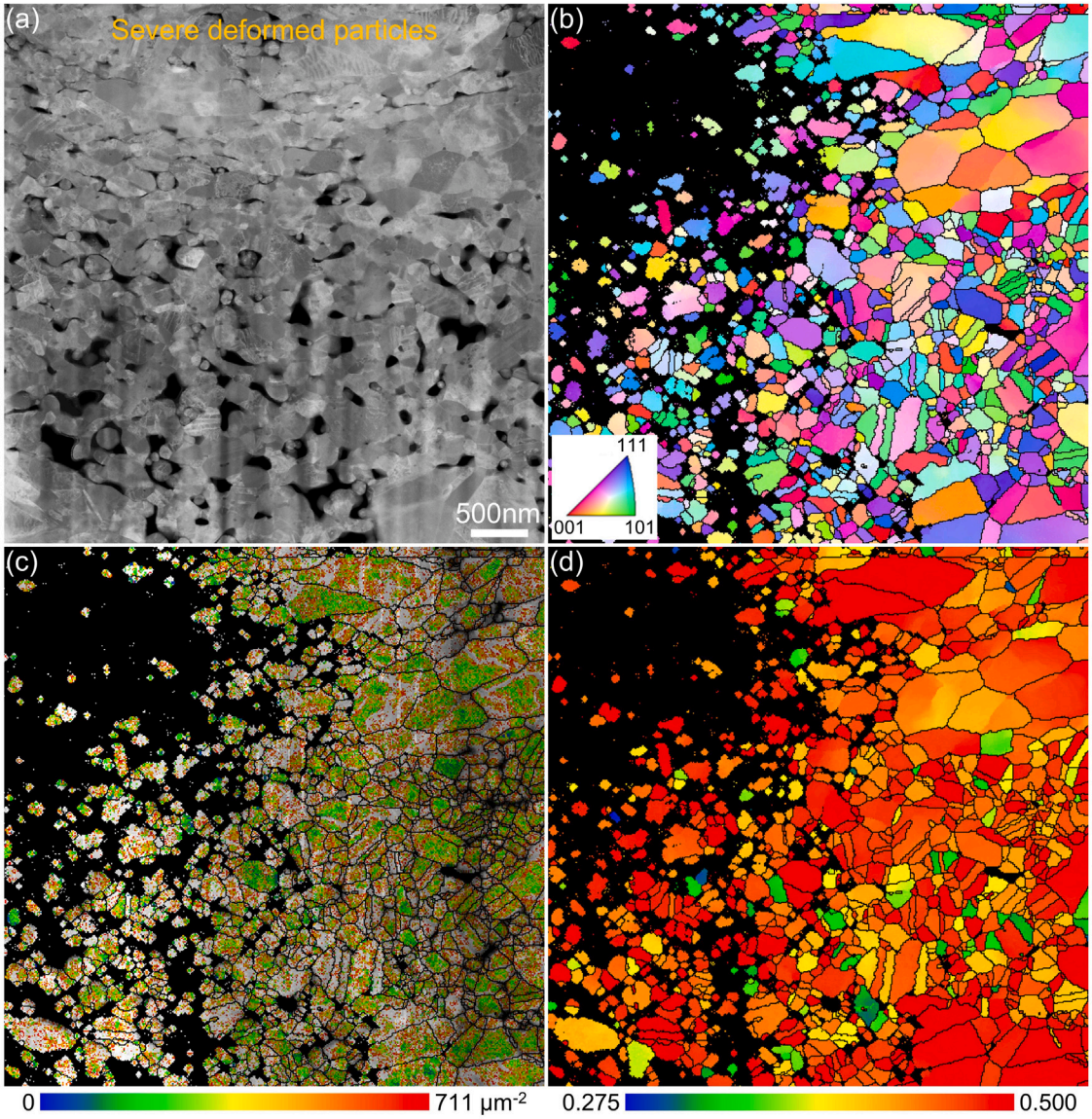

Fig. 9. Deformation mechanism of sintered Cu NP micro-pillar after compression: (a) STEM image showing severely deformed particles in the top region; (b) inverse pole figure (IPF) map revealing a random distribution of crystallographic orientations; (c) GNDs density map; (d) Schmid factor map.

and nanocrystalline counterparts [72,73]. Unlike bulk Cu, where plasticity is typically governed by well-defined slip along specific crystallographic planes, the sintered Cu NPs undergo a two-stage deformation process driven by their porous architecture and heterogeneous grain structure. Initially, compressive stress leads to the compaction of the porous network, forming dense particle–particle contacts. This process reduces the effective stiffness (elastic modulus) of the material, a characteristic beneficial for applications such as electronic packaging where compliance with thermal expansion mismatch is critical [81]. Following the initial compaction stage, plastic deformation in sintered Cu NPs is primarily accommodated through intragranular slip within individual particles. The randomly distributed crystallographic orientations, as revealed by TKD analysis, lead to independent activation of multiple slip systems across different grains. This crystallographic heterogeneity promotes distributed plasticity and suppresses the formation of localized shear bands typically observed in textured or single-slip dominated structures, thereby enhancing ductility and delaying catastrophic failure [82]. The dislocations accumulate at particle interfaces and form entangled networks that obstruct further dislocation motion, effectively increasing resistance to continued plastic flow [83]. This dislocation-based interaction acts as a secondary hardening mechanism, sustaining strain hardening throughout the deformation process and contributing to the overall mechanical robustness of the porous sintered structure.

Crucially, the deformation behavior is governed not only by differences in crystallographic orientation but also by particle size heterogeneity. Large particles, owing to their extended slip paths and reduced boundary confinement, more readily accommodate intragranular plasticity and sustain significant plastic strain [84]. In contrast, smaller particles—typically situated at particle junctions or constrained interstitial sites—exhibit limited plasticity due to geometric confinement and high grain boundary density. These features enhance their mechanical rigidity, enabling them to pin dislocations and act as local load-bearing units that resist premature yielding [85].

The tri-level interplay—between particle size, orientation, and porosity—produces a synergistic energy dissipation framework. It not only enhances load transfer and impedes crack propagation but also suppresses strain localization by activating diverse deformation pathways [86]. As a result, sintered Cu NPs achieve an exceptional combination of high strength (250–350 MPa) and low elastic modulus (20

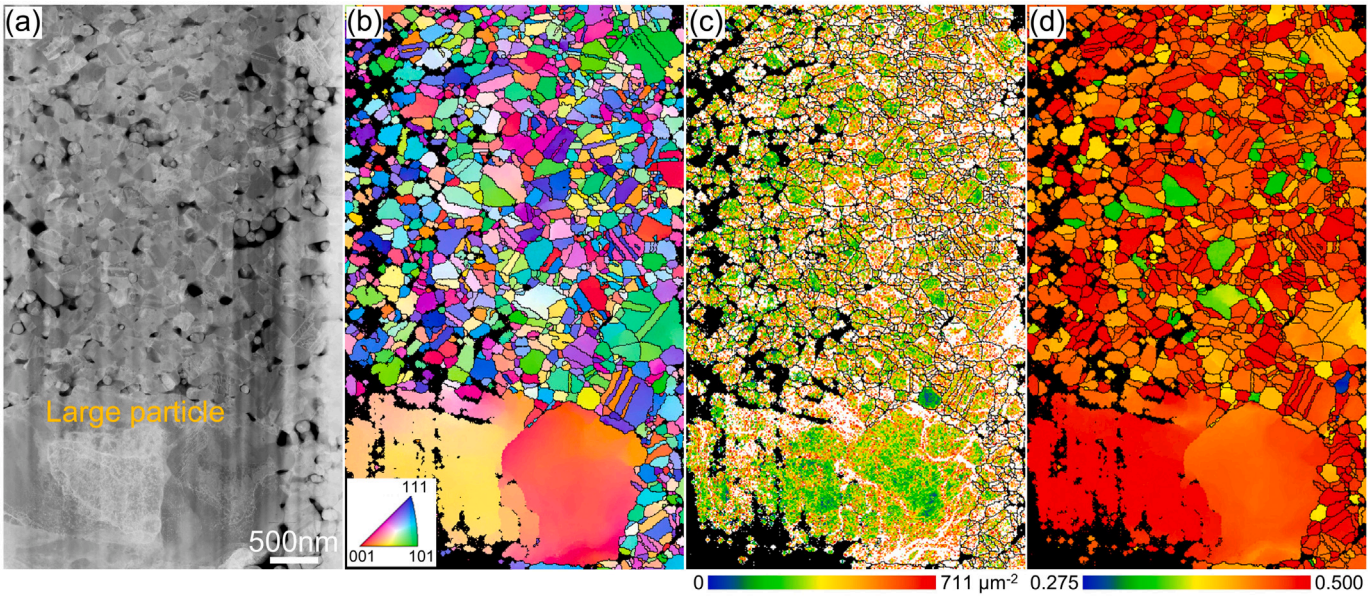

Fig. 10. Deformation mechanism of sintered Cu NP micro-pillar after compression: (a) STEM image showing both nano- and microparticles; (b) inverse pole figure (IPF) map; (c) GNDs density map; (d) Schmid factor map.

GPa). In contrast, fully dense nanocrystalline Cu often exhibits limited strain hardening due to grain boundary-mediated softening mechanisms such as sliding and rotation [87]. The distinctive processing–structure–property relationship of sintered Cu NPs underscores the dual role of porosity and particle heterogeneity in simultaneously enhancing compliance and mechanical robustness, offering a scalable design paradigm for advanced metallic systems subjected to complex loading and thermal cycling conditions.

4.2. Microstructure evolution during sintering by MD simulation

To further reveal the evolution of the hierarchical microstructure, MD simulation for the sintering process of bimodal particle models is presented in Fig. 11. In the initial stage after heating to 250 °C (Fig. 11a1), small particles coalesce significantly, and the large particles attract smaller particles due to localized capillary forces [88]. This early-stage sintering shows minimal dislocation activity, as seen in Fig. 11a2, since thermal effects dominate and mechanical deformation is negligible. However, as strain increases to 20% (Fig. 11b1), stress-induced diffusion becomes dominant, particularly near large particles. The denser structure near these earlier contact regions reflects enhanced atomic diffusion facilitated by localized stress and thermal activation. At 40% strain (Fig. 11c1), the sintering process accelerates further, leading to enhanced densification and reduced porosity, particularly in regions between large particles where small particles form significant sintered necks. This mechanism aligns with the experimental findings (Figs. 4 and 5), where reduced porosity and enhanced densification were observed near large particles under applied pressure. With increasing strain, dislocation density rises significantly and stacking faults begin to form, particularly within large particles (Figs. 11b2, c2). This reflects localized stress redistribution and strain accumulation during deformation [89]. The resulting dislocation structures and planar defects enhance interfacial contact and promote particle interlocking, thereby facilitating sintering neck growth and improving structural cohesion.

To investigate the effect of the relative positioning of large and small particles on the sintered microstructure, the sintering process was simulated using the same initial particle model under X- and Y-directional pressures at 30% and 40% strain, enabling a comparative analysis of the compaction behavior (Fig. 12). At 40% strain, the microstructure becomes denser, with smaller and more uniformly distributed voids compared to 30% strain, indicating that higher strain promotes enhanced particle rearrangement and densification. The stacking fault distributions (second column in Fig. 12) increase with strain and are primarily localized near large particles and sintered necks. This reflects stress-induced plasticity, where localized slip contributes to stress relaxation and interparticle accommodation [90]. Likewise, the dislocation density (third column in Fig. 12) rises progressively with strain, with pronounced accumulation around large particles and neck regions. This dislocation activity signifies ongoing plastic deformation, which aids in relieving local stress and enabling atomic rearrangement at interfaces [91]. Moreover, the observed anisotropy in defect distributions between the X and Y directions underscores the role of initial particle configuration in shaping the local stress field and guiding microstructural evolution during deformation.

4.3. Tensile and compressive behavior by MD simulation

The mechanical response of sintered particle models under tensile and compressive conditions, along with the corresponding fracture morphologies, is presented in Fig. 13. This figure highlights the influence of sintering strain (30%, 40% and 50%) and sintering direction on both tensile and compressive behavior, revealing critical insights into the interplay between microstructure and mechanical properties. The stress–strain curves under tensile loading (Fig. 13a) show that tensile strength strongly depends on the sintering strain. As the sintering strain increases from 30% to 50%, the tensile strength improves significantly, reflecting the progressive densification and enhanced interparticle bonding. This improvement is attributed to the formation of stronger sintered necks and reduced porosity, which enhance load transfer across particles. However, the fracture morphology (Figs. 13c1, c2, d1, d2) reveals that failure predominantly occurs in regions where small particles are accumulated. This observation confirms the insufficient sintering of small particles, which can be attributed to a stress shielding effect induced by large particles [92]. Notably, as the sintering strain increases, the fracture surface location changes. For example, Figs. 13d1 and d2 show that at higher sintering strain (50%), the fracture surface shifts compared to 40%. This shift suggests that the most vulnerable regions evolve with increasing densification, as stress redistribution occurs within the microstructure. The local stress

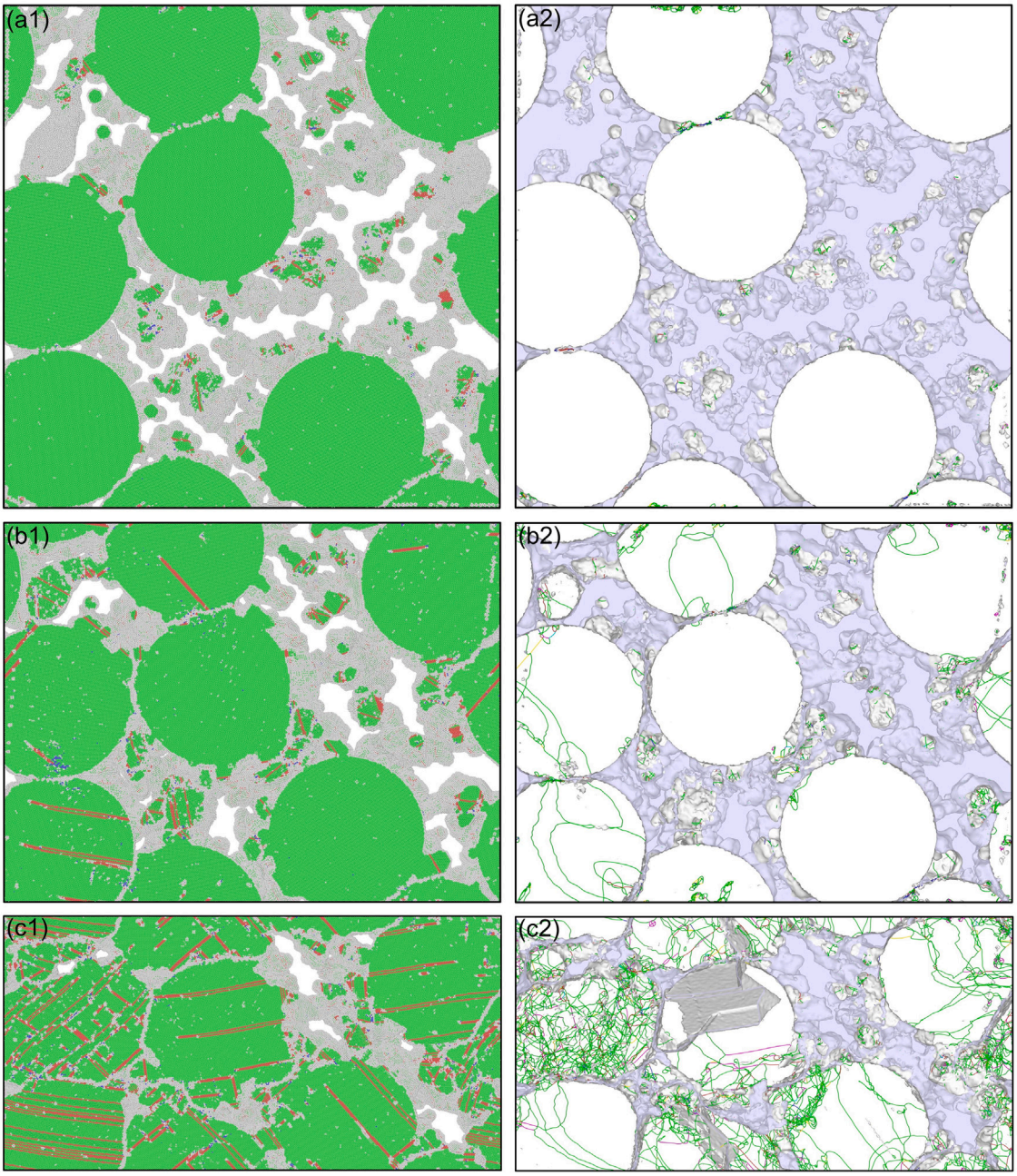

Fig. 11. Evolution of the microstructure and dislocation distribution during the sintering process: (a1, a2) Initial particle morphology after the temperature rises to 250 °C; (b1, b2) microstructure at 20% strain during sintering; (c1, c2) microstructure at 40% strain during sintering.

concentration around partially sintered small particles may lead to a transition in fracture pathways.

Fig. 13b shows that the stress–strain curves under compressive loading also exhibit a strong dependence on the sintering strain. At lower sintering strains (30%), the stress–strain curves exhibit a progressive increase in stress with strain, but without a clear yield stage. This behavior can be attributed to the initial high porosity and incomplete sintering, where the applied stress primarily compacts the porous structure, resulting in densification and a corresponding increase in strength. The lack of a well-defined yield stage indicates that deformation in this regime is dominated by porosity compaction. At higher sintering strains (40% and 50%), the stress–strain curves exhibit a more pronounced yield stage. The higher sintering strain produces a denser microstructure with reduced porosity and well-formed sintered necks, which can better sustain compressive loads. The simulation results align well with the experimental findings. Under compressive loading, large particles accommodate intragranular slip and act as the initial sites for plastic deformation, thereby absorbing early strain energy. Localized stress maps (Figs. S3–S4) confirm that these large particles, together with sintered necks, are the primary stress concentration sites where dislocations and stacking faults preferentially nucleate. This defect activity subsequently redistributes strain energy, highlighting their dual role as both markers of stress concentration and effective stress relaxation pathways. In contrast, small particles—often situated at interstitial or constrained sites—undergo densification and shear-compression, which enhances load transfer, bridges particle interfaces, and suppresses excessive localized deformation. The combined action of large and small particles thus facilitates a more uniform strain distribution and promotes structural integrity during sintering and deformation. The compressive morphologies shown in Figs. 13e1, e2,

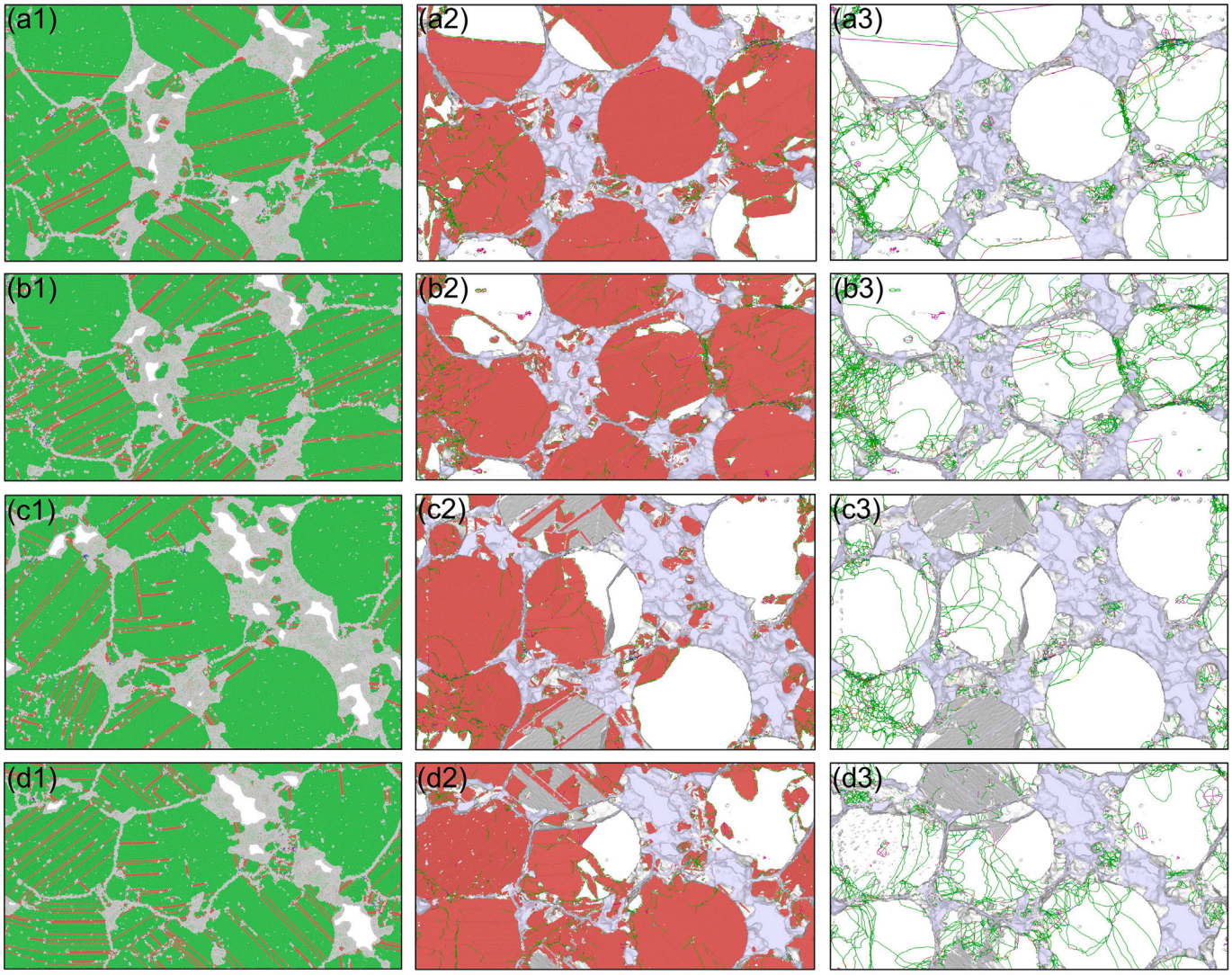

Fig. 12. Evolution of microstructure, stacking faults and dislocations in particle models sintered under pressure along the X and Y directions: (a1–b1) Microstructure morphology at 30% and 40% strain along the X direction; (c1–d1) microstructure morphology at 30% and 40% strain along the Y direction; (a2–d2) corresponding stacking fault distributions, indicating increased fault activity with strain; (a3–d3) corresponding dislocation distributions, showing progressive accumulation and concentration of dislocations around particle boundaries and sintered necks during sintering.

f1, f2, together with the stress distributions in Figs. S3–S4, support this interpretation by demonstrating that particle size governs both the initiation of stress concentration and the subsequent pathways of plastic accommodation.

5. Conclusion

This study establishes a clear relationship between sintering pressure, microstructure evolution and the resulting mechanical strength of sintered Cu NPs, providing a fundamental understanding of the underlying mechanisms. The main findings are as follows:

1. The applied sintering pressure significantly promotes sintered neck formation and reduces porosity in Cu NPs. Under constrained temperature (250 °C), time (5 min) and pressure conditions (0–30 MPa), the sintered structure reaches a densification plateau. In this study, optimal densification was achieved at 20 MPa, resulting in a reduction in porosity to 7% and the formation of robust sintering necks.

2. Sintered Cu NPs exhibit a desirable combination of high strength and low elastic modulus, making them well-suited for electronic packaging applications. As sintering pressure increases from 0 to 30 MPa, the yield strength improves significantly, rising from 120 MPa to over 320 MPa. Concurrently, the elastic modulus increases from 4.8 GPa to 20 GPa. Moreover, the failure mode transitions from collapse driven by weak interparticle adhesion and poor neck formation to compaction-dominated deformation characterized by well-developed necks and reduced porosity.

3. Sintered Cu NPs exhibit a two-stage deformation mechanism governed by their porous architecture and heterogeneous microstructure. Initially, compressive loading induces voids compaction, and establishing dense interparticle contacts. Subsequently, plastic deformation is accommodated primarily through intragranular slip. A synergistic interplay among particle size, crystallographic orientation, and porosity enables efficient energy dissipation, enhancing load transfer, suppressing strain localization, and impeding crack propagation through the activation of multiple deformation pathways.

4. MD simulations demonstrate that the mechanical behavior of sintered Cu nanoparticle assemblies is governed by a size-dependent synergy between large and small particles, modulated by sintering strain. Under tension, increased sintering strain enhances strength through

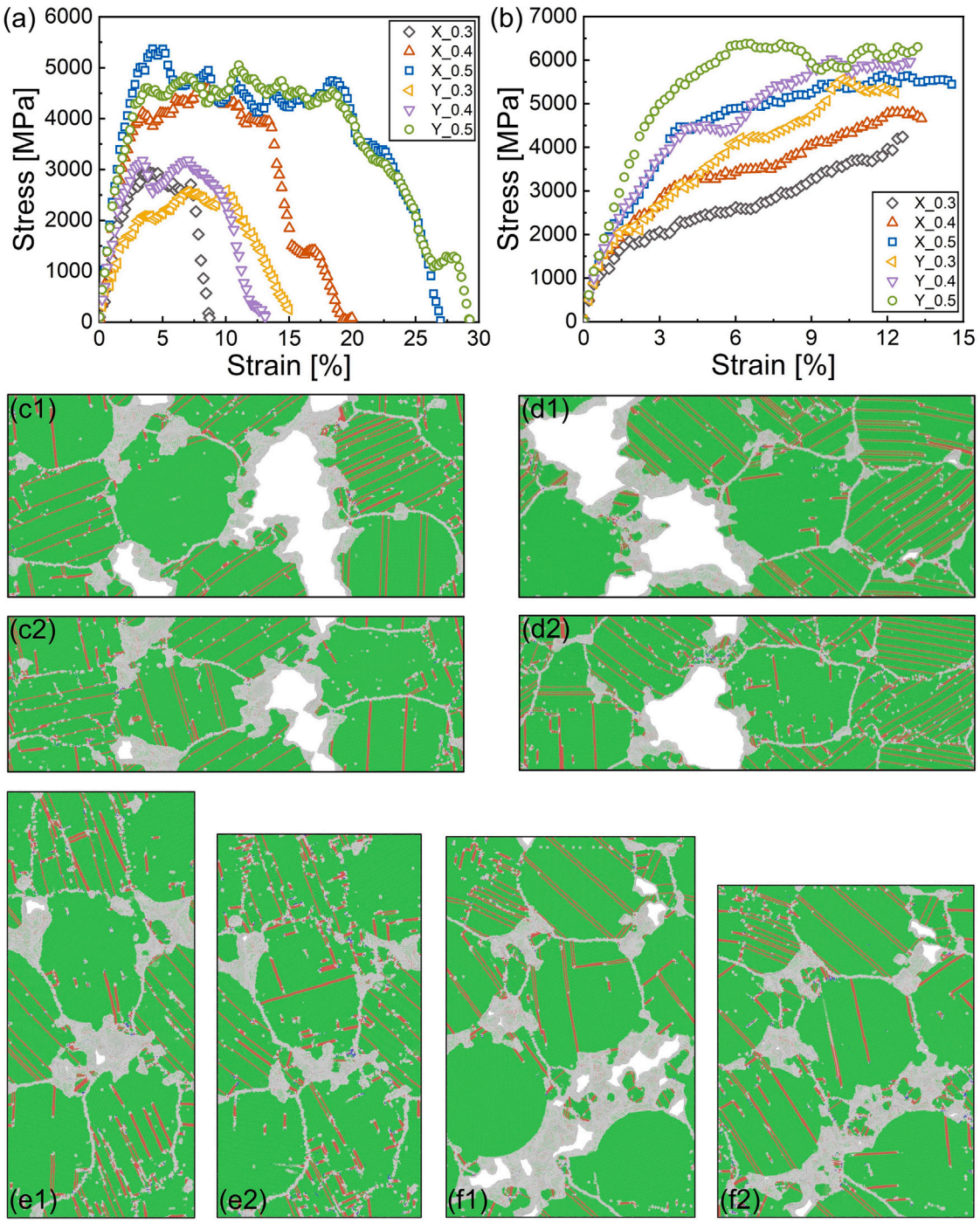

Fig. 13. Stress–strain curves and corresponding deformed morphologies of sintered particle models under tensile and compressive conditions obtained from MD simulations: (a) Tensile stress–strain curves; (b) compressive stress–strain curves; (c1, c2) fracture morphologies after tensile loading along the X direction for models sintered under 40% and 50% strain along the Y direction, respectively; (d1, d2) fracture morphologies after tensile loading along the Y direction for models sintered under 40% and 50% strain along the X direction, respectively; (e1, e2) compressive morphologies along the X direction for the model sintered with 50% strain; (f1, f2) compressive morphologies along the Y direction for the model sintered with 30% strain.

densification and improved bonding, but fracture preferentially initiates in small-particle-rich regions due to stress shielding and incomplete sintering. In compression, deformation involves intragranular slip in large particles and densification in small particles, enabling effective load transfer and suppressing strain localization. This cooperative mechanism underpins the enhanced structural integrity of the sintered porous architecture, highlighting the critical role of particle size distribution and local bonding in governing mechanical performance.

In summary, this study elucidates the deformation mechanisms underlying the unique combination of high strength and low elastic modulus in sintered Cu NPs, arising from their hierarchical microstructure. The findings highlight a distinctive processing–structure–property relationship, wherein porosity and particle heterogeneity jointly enhance mechanical compliance and robustness. This dual functionality offers a scalable design strategy for advanced metallic systems operating under complex mechanical and thermal loading conditions.

CRediT authorship contribution statement

Leiming Du: Writing – original draft, Methodology, Investigation, Formal analysis, Data curation, Conceptualization. **Gerald Schaffar:** Methodology, Investigation. **Weiping Jiao:** Methodology, Investigation. **Kai Liu:** Methodology, Investigation. **René H. Poelma:** Writing – review & editing, Supervision. **Verena Maier-Kiener:** Writing – review & editing, Supervision, Methodology. **Jiajie Fan:** Writing – review & editing, Supervision. **Daniel Kiener:** Writing – review & editing, Supervision. **Willem D. van Driel:** Writing – review & editing, Supervision. **Xuejun Fan:** Writing – review & editing, Supervision. **Guoqi Zhang:** Writing – review & editing, Supervision.

Declaration of competing interest

The authors declare that they have no known competing financial interests or personal relationships that could have appeared to influence the work reported in this paper.

Acknowledgments

The authors would like to acknowledge the financial support from the ECSEL Joint Undertaking (JU) under grant agreement No 876659. The JU receives support from the European Union's Horizon 2020 research and innovation program and Germany, Austria, Slovakia, Sweden, Finland, Belgium, Italy, Spain, Netherlands, Slovenia, Greece, France, and Turkey. For the Titan TEM results, we acknowledge support from the Kavli Institute of Nanoscience, Delft University of Technology, and the Netherlands Electron Microscopy Infrastructure (NEMI), project number 184.034.014, part of the National Roadmap and financed by the Dutch Research Council (NWO).

Appendix A. Supplementary data

Supplementary material related to this article can be found online at https://doi.org/10.1016/j.actamat.2025.121501.

References

[1] J. Liu, H. Chen, H. Ji, M. Li, Highly conductive cu–cu joint formation by low-temperature sintering of formic acid-treated cu nanoparticles, ACS Appl. Mater. Interfaces 8 (48) (2016) 33289–33298.
[2] Y. Dai, M. Ng, P. Anantha, Y. Lin, Z. Li, C. Gan, C. Tan, Enhanced copper micro/nano-particle mixed paste sintered at low temperature for 3D interconnects, Appl. Phys. Lett. 108 (26) (2016).
[3] J.E. Morris, Nanopackaging: Nanotechnologies and electronics packaging, Springer, 2018.
[4] Y. Wang, D. Xu, H. Yan, C.-F. Li, C. Chen, W. Li, Low-temperature copper sinter-joining technology for power electronics packaging: A review, J. Mater. Process. Technol. (2024) 118526.
[5] Y. Zuo, C. Zhao, A. Robador, M. Wickham, S.H. Mannan, Quasi-in-situ observation of the grain growth and grain boundary movement in sintered cu nanoparticle interconnects, Acta Mater. 236 (2022) 118135.
[6] M.R. Akbarpour, F. Gazani, H.M. Mirabad, I. Khezri, A. Moeini, N. Sohrabi, H.S. Kim, Recent advances in processing, and mechanical, thermal and electrical properties of cu-SiC metal matrix composites prepared by powder metallurgy, Prog. Mater. Sci. (2023) 101191.
[7] N.K. Roy, C.S. Foong, M.A. Cullinan, Effect of size, morphology, and synthesis method on the thermal and sintering properties of copper nanoparticles for use in microscale additive manufacturing processes, Addit. Manuf. 21 (2018) 17–29.
[8] Z. Cui, Q. Jia, Y. Wang, D. Li, C.-P. Wang, H. Zhang, Z. Lu, L. Ma, G. Zou, F. Guo, Enhanced shear strength and microstructure of cu–cu interconnection by low-temperature sintering of cu nanoparticles, J. Mater. Sci., Mater. Electron. 35 (11) (2024) 1–13.
[9] H. Lyu, C. Wang, K. Li, X. Jia, J. He, D. Yan, N. Lin, et al., Sintering and optimization of copper nanopaste-connected copper array conical microstructures, Mater. Sci. Semicond. Process. 186 (2025) 109081.
[10] A. Malti, A. Kardani, A. Montazeri, An insight into the temperature-dependent sintering mechanisms of metal nanoparticles through MD-based microstructural analysis, Powder Technol. 386 (2021) 30–39.
[11] B. Hou, H.-J. Huang, C.-M. Wang, M.-B. Zhou, X.-P. Zhang, Superb sinterability of the cu paste consisting of bimodal size distribution cu nanoparticles for low-temperature and pressureless sintering of large-area die attachment and the sintering mechanism, in: 2022 IEEE 72nd Electronic Components and Technology Conference, ECTC, IEEE, 2022, pp. 2064–2070.
[12] Z. Ni, Y. Liu, F. Ye, Formation of ultrasonic spot welded Cu/Cu NPs/cu joints and the mechanical properties and electrical resistance, Mater. Sci. Eng.: A 845 (2022) 143251.
[13] X. Liu, S. Li, J. Fan, J. Jiang, Y. Liu, H. Ye, G. Zhang, Microstructural evolution, fracture behavior and bonding mechanisms study of copper sintering on bare DBC substrate for SiC power electronics packaging, J. Mater. Res. Technol. 19 (2022) 1407–1421.
[14] D. Dai, J. Qian, J. Li, Y. Huang, Z. Wang, J. Yu, X. Wang, X. Chen, A rapid-sintering cu-cu joints with ultrahigh shear strength and super reliability for power electronics package, Mater. Sci. Semicond. Process. 178 (2024) 108405.
[15] K. Wakamoto, D. Yasugi, T. Otsuka, K. Nakahara, T. Namazu, Fracture mechanism of sintered silver film revealed by in-situ sem uniaxial tensile loading, IEEE Trans. Components Packag. Manufacturing Technol. (2024).
[16] B. Li, J. Wang, Y. Yao, Creep behavior of sintered nano-silver at high temperature: Experimental and theoretical analysis, Mater. Today Commun. 37 (2023) 106956.
[17] D. Kiener, A. Misra, Nanomechanical characterization, MRS Bull. 49 (3) (2024) 214–223.
[18] C. Chen, S. Nagao, K. Suganuma, J. Jiu, T. Sugahara, H. Zhang, T. Iwashige, K. Sugiura, K. Tsuruta, Macroscale and microscale fracture toughness of microporous sintered ag for applications in power electronic devices, Acta Mater. 129 (2017) 41–51.
[19] D. Kiener, M. Wurmshuber, M. Alfreider, G.J. Schaffar, V. Maier-Kiener, Recent advances in nanomechanical and in situ testing techniques: Towards extreme conditions, Curr. Opin. Solid State Mater. Sci. 27 (6) (2023) 101108.
[20] D. Hu, L. Du, M. Alfreider, J. Fan, D. Kiener, G. Zhang, Microscopic fracture toughness of notched porous sintered cu micro-cantilevers for power electronics packaging, Mater. Sci. Eng.: A 897 (2024) 146316.
[21] D. Kiener, P. Guruprasad, S.M. Keralavarma, G. Dehm, A.A. Benzerga, Work hardening in micropillar compression: In situ experiments and modeling, Acta Mater. 59 (10) (2011) 3825–3840.
[22] R.H. Poelma, B. Morana, S. Vollebregt, E. Schlangen, H.W. van Zeijl, X. Fan, G.Q. Zhang, Tailoring the mechanical properties of high-aspect-ratio carbon nanotube arrays using amorphous silicon carbide coatings, Adv. Funct. Mater. 24 (36) (2014) 5737–5744.
[23] R.H. Poelma, X. Fan, Z.-Y. Hu, G. Van Tendeloo, H.W. van Zeijl, G.Q. Zhang, Effects of nanostructure and coating on the mechanics of carbon nanotube arrays, Adv. Funct. Mater. 26 (8) (2016) 1233–1242.
[24] X. Milhet, A. Nait-Ali, D. Tandiang, Y.-J. Liu, D. Van Campen, V. Caccuri, M. Legros, Evolution of the nanoporous microstructure of sintered ag at high temperature using in-situ X-ray nanotomography, Acta Mater. 156 (2018) 310–317.
[25] J. Wu, Y. Chiu, Y. Wang, C. Kao, Mechanical characterizations of single-crystalline (cu, Ni) 6sn5 through uniaxial micro-compression, Mater. Sci. Eng.: A 753 (2019) 22–30.
[26] C. Chen, K. Suganuma, Microstructure and mechanical properties of sintered ag particles with flake and spherical shape from nano to micro size, Mater. Des. 162 (2019) 311–321.
[27] M. Zhang, X. Wang, A.D. Dupuy, J.M. Schoenung, X. Li, Study on strain rate–dependent deformation mechanism of WC–10 wt% Ni3Al cemented carbide by micropillar compression, Adv. Eng. Mater. 22 (3) (2020) 1900953.
[28] M. Hamid, M.S. Saleh, A. Afrouzian, R. Panat, H.M. Zbib, Modeling of porosity and grain size effects on mechanical behavior of additively manufactured structures, Addit. Manuf. 38 (2021) 101833.
[29] R. Ramachandramoorthy, S. Kalácska, G. Poras, J. Schwiedrzik, T.E. Edwards, X. Maeder, T. Merle, G. Ercolano, W.W. Koelmans, J. Michler, Anomalous high strain rate compressive behavior of additively manufactured copper micropillars, Appl. Mater. Today 27 (2022) 101415.
[30] S.-H. Li, Y. Zhao, J. Radhakrishnan, U. Ramamurty, A micropillar compression investigation into the plastic flow properties of additively manufactured alloys, Acta Mater. 240 (2022) 118290.
[31] Z. Wang, Z. Song, W. Luo, T. Shang, Z. Liu, J. Yuan, X. Fan, Y. Zhu, The effect of temperature on the mechanisms of cu nanoparticle sintering: A molecular dynamic study, Powder Technol. 440 (2024) 119802.
[32] J. Liu, W. Lv, C. Chen, Y. Kang, Atomic insight in fusion mechanism of heterogeneous and homogeneous sintering: Cu and Ag nanoparticles, Results Phys. 57 (2024) 107411.
[33] Y.U. Wang, Computer modeling and simulation of solid-state sintering: A phase field approach, Acta Mater. 54 (4) (2006) 953–961.
[34] K. Shinagawa, Simulation of grain growth and sintering process by combined phase-field/discrete-element method, Acta Mater. 66 (2014) 360–369.

[35] B. Dzepina, D. Balint, D. Dini, A phase field model of pressure-assisted sintering, J. Eur. Ceram. Soc. 39 (2–3) (2019) 173–182.
[36] J. Hötzer, M. Seiz, M. Kellner, W. Rheinheimer, B. Nestler, Phase-field simulation of solid state sintering, Acta Mater. 164 (2019) 184–195.
[37] S. Hara, A. Ohi, N. Shikazono, Sintering analysis of sub-micron-sized nickel powders: Kinetic Monte Carlo simulation verified by FIB–SEM reconstruction, J. Power Sources 276 (2015) 105–112.
[38] Y. Zhang, X. Xiao, J. Zhang, Kinetic Monte Carlo simulation of sintering behavior of additively manufactured stainless steel powder particles using reconstructed microstructures from synchrotron X-ray microtomography, Results Phys. 13 (2019) 102336.
[39] S. Zhou, X. Liu, Z. Yan, S. Hara, N. Shikazono, Z. Zhong, Kinetic Monte Carlo (KMC) simulation of sintering of nickel oxide-yttria stabilized zirconia composites: Model, parameter calibration and validation, Mater. Des. 232 (2023) 112094.
[40] F. Wakai, M. Yoshida, Y. Shinoda, T. Akatsu, Coarsening and grain growth in sintering of two particles of different sizes, Acta Mater. 53 (5) (2005) 1361–1371.
[41] K.-i. Mori, Finite element simulation of powder forming and sintering, Comput. Methods Appl. Mech. Engrg. 195 (48–49) (2006) 6737–6749.
[42] H. Ch'ng, J. Pan, Sintering of particles of different sizes, Acta Mater. 55 (3) (2007) 813–824.
[43] C. Martin, L. Schneider, L. Olmos, D. Bouvard, Discrete element modeling of metallic powder sintering, Scr. Mater. 55 (5) (2006) 425–428.
[44] B. Henrich, A. Wonisch, T. Kraft, M. Moseler, H. Riedel, Simulations of the influence of rearrangement during sintering, Acta Mater. 55 (2) (2007) 753–762.
[45] B. Paredes-Goyes, D. Jauffres, J.-M. Missiaen, C.L. Martin, Grain growth in sintering: A discrete element model on large packings, Acta Mater. 218 (2021) 117182.
[46] B. Paredes-Goyes, A.M. Venkatesh, D. Jauffres, C.L. Martin, Two-step sintering of alumina nano-powders: A discrete element study, J. Eur. Ceram. Soc. 43 (2) (2023) 501–509.
[47] M.W. Reiterer, K.G. Ewsuk, An analysis of four different approaches to predict and control sintering, J. Am. Ceram. Soc. 92 (7) (2009) 1419–1427.
[48] J. Liu, W. Lv, Y. Mou, C. Chen, Y. Kang, Coalescence behavior of cu nanoparticles during sintering: Based on atomic scale to macro scale, J. Mater. Res. Technol. 27 (2023) 2490–2507.
[49] A. Averardi, C. Cola, S.E. Zeltmann, N. Gupta, Effect of particle size distribution on the packing of powder beds: A critical discussion relevant to additive manufacturing, Mater. Today Commun. 24 (2020) 100964.
[50] M.R. Mazlan, N.H. Jamadon, A. Rajabi, A.B. Sulong, I.F. Mohamed, F. Yusof, N.A. Jamal, Necking mechanism under various sintering process parameters–a review, J. Mater. Res. Technol. 23 (2023) 2189–2201.
[51] L. Ma, Z. Lu, Q. Jia, Z. Cui, Y. Wang, D. Li, H. Zhang, G. Zou, F. Guo, Sintering mechanism of bimodal-sized cu nanoparticle paste for power electronics packaging, J. Electron. Mater. 53 (6) (2024) 2988–2998.
[52] X. Jingxiang, H. Yuji, O. Nobuki, S. Kazuhisa, H. Toshiyuki, K. Momoji, Parallel large-scale molecular dynamics simulation opens new perspective to clarify the effect of a porous structure on the sintering process of Ni/YSZ multiparticles, 2017.
[53] P. Liang, Z. Pan, L. Tang, G. Zhang, D. Yang, S. He, H. Yan, Molecular dynamics simulation of sintering densification of multi-scale silver layer, Materials 15 (6) (2022) 2232.
[54] G.J. Schaffar, D. Tscharnuter, V. Maier-Kiener, Exploring the high-temperature deformation behavior of monocrystalline silicon–an advanced nanoindentation study, Mater. Des. 233 (2023) 112198.
[55] A.J. Leide, R.I. Todd, D.E. Armstrong, Measurement of swelling-induced residual stress in ion implanted SiC, and its effect on micromechanical properties, Acta Mater. 196 (2020) 78–87.
[56] S. Huang, Q. Zhao, C. Lin, C. Wu, Y. Zhao, W. Jia, C. Mao, In-situ investigation of tensile behaviors of Ti–6Al alloy with extra low interstitial, Mater. Sci. Eng.: A 809 (2021) 140958.
[57] A.A. Saleh, G. Casillas, E.V. Pereloma, K.R. Carpenter, C.R. Killmore, A.A. Gazder, A transmission kikuchi diffraction study of cementite in a quenched and tempered steel, Mater. Charact. 114 (2016) 146–150.
[58] B.M. Jenkins, J.O. Douglas, H.M. Gardner, D. Tweddle, A. Kareer, P.S. Karamched, N. Riddle, J.M. Hyde, P.A. Bagot, G.R. Odette, et al., A more holistic characterisation of internal interfaces in a variety of materials via complementary use of transmission kikuchi diffraction and atom probe tomography, Appl. Surf. Sci. 528 (2020) 147011.
[59] A.P. Thompson, H.M. Aktulga, R. Berger, D.S. Bolintineanu, W.M. Brown, P.S. Crozier, P.J. In't Veld, A. Kohlmeyer, S.G. Moore, T.D. Nguyen, et al., LAMMPS-a flexible simulation tool for particle-based materials modeling at the atomic, meso, and continuum scales, Comput. Phys. Comm. 271 (2022) 108171.
[60] A. Stukowski, Visualization and analysis of atomistic simulation data with OVITO–the open visualization tool, Modelling Simul. Mater. Sci. Eng. 18 (1) (2009) 015012.
[61] Y. Mishin, M. Mehl, D. Papaconstantopoulos, A. Voter, J. Kress, Structural stability and lattice defects in copper: Ab initio, tight-binding, and embedded-atom calculations, Phys. Rev. B 63 (22) (2001) 224106.
[62] D.E. Spearot, M.A. Tschopp, K.I. Jacob, D.L. McDowell, Tensile strength of< 1 0 0 > and < 1 1 0 > tilt bicrystal copper interfaces, Acta Mater. 55 (2) (2007) 705–714.
[63] J. Suryawanshi, G. Singh, S. Msolli, M.H. Jhon, U. Ramamurty, Tension-compression asymmetry and shear strength of titanium alloys, Acta Mater. 221 (2021) 117392.
[64] J. Zhang, G. Liu, J. Sun, Strain rate effects on the mechanical response in multi- and single-crystalline cu micropillars: Grain boundary effects, Int. J. Plast. 50 (2013) 1–17.
[65] X. Zhao, J. Wu, Y. Chiu, I. Jones, R. Gu, A. Ngan, Critical dimension for the dislocation structure in deformed copper micropillars, Scr. Mater. 163 (2019) 137–141.
[66] S. Kalácska, Z. Dankházi, G. Zilahi, X. Maeder, J. Michler, P.D. Ispánovity, I. Groma, Investigation of geometrically necessary dislocation structures in compressed cu micropillars by 3-dimensional HR-EBSD, Mater. Sci. Eng.: A 770 (2020) 138499.
[67] D. Xie, M.-J. Chen, J. Gigax, D. Luscher, J. Wang, A. Hunter, S. Fensin, M. Zikry, N. Li, A fundamental understanding of how dislocation densities affect strain hardening behavior in copper single crystalline micropillars, Mech. Mater. 184 (2023) 104731.
[68] T. Hirouchi, Y. Shibutani, Mechanical responses of copper bicrystalline micro pillars with $\sigma 3$ coherent twin boundaries by uniaxial compression tests, Mater. Trans. 55 (1) (2014) 52–57.
[69] P.J. Imrich, C. Kirchlechner, C. Motz, G. Dehm, Differences in deformation behavior of bicrystalline cu micropillars containing a twin boundary or a large-angle grain boundary, Acta Mater. 73 (2014) 240–250.
[70] C. Kirchlechner, F. Toth, F.G. Rammerstorfer, F.D. Fischer, G. Dehm, Pre-and post-buckling behavior of bi-crystalline micropillars: Origin and consequences, Acta Mater. 124 (2017) 195–203.
[71] C. Howard, D. Frazer, A. Lupinacci, S. Parker, R. Valiev, C. Shin, B.W. Choi, P. Hosemann, Investigation of specimen size effects by in-situ microcompression of equal channel angular pressed copper, Mater. Sci. Eng.: A 649 (2016) 104–113.
[72] J. Zhang, G. Liu, J. Sun, Comparisons between homogeneous boundaries and heterophase interfaces in plastic deformation: Nanostructured Cu micropillars vs. nanolayered Cu-based micropillars, Acta Mater. 61 (18) (2013) 6868–6881.
[73] N.L. Okamoto, D. Kashioka, T. Hirato, H. Inui, Specimen-and grain-size dependence of compression deformation behavior in nanocrystalline copper, Int. J. Plast. 56 (2014) 173–183.
[74] M. Mutoh, T. Nagoshi, T.-F.M. Chang, T. Sato, M. Sone, Micro-compression test using non-tapered micro-pillar of electrodeposited cu, Microelectron. Eng. 111 (2013) 118–121.
[75] X. Zhang, H. Wang, F. Ye, C. Zou, Z. Wei, Cooperative effect of Mg and si contents on the microstructural evolution, mechanical performance, and deformation behavior of cast Al–Li–Mg–Si alloys, Mater. Sci. Eng.: A 841 (2022) 142976.
[76] M.D. Sangid, T. Ezaz, H. Sehitoglu, I.M. Robertson, Energy of slip transmission and nucleation at grain boundaries, Acta Mater. 59 (1) (2011) 283–296.
[77] T. Zhang, J. Jiang, B.A. Shollock, T.B. Britton, F.P. Dunne, Slip localization and fatigue crack nucleation near a non-metallic inclusion in polycrystalline nickel-based superalloy, Mater. Sci. Eng.: A 641 (2015) 328–339.
[78] D. Norfleet, D. Dimiduk, S. Polasik, M. Uchic, M. Mills, Dislocation structures and their relationship to strength in deformed nickel microcrystals, Acta Mater. 56 (13) (2008) 2988–3001.
[79] S. Queyreau, G. Monnet, B. Devincre, Orowan strengthening and forest hardening superposition examined by dislocation dynamics simulations, Acta Mater. 58 (17) (2010) 5586–5595.
[80] H. Zhong, Q. Shi, C. Dan, X. You, S. Zong, S. Zhong, Y. Zhang, H. Wang, Z. Chen, Resolving localized geometrically necessary dislocation densities in al-mg polycrystal via in situ EBSD, Acta Mater. 279 (2024) 120290.
[81] M. Amagai, Mechanical reliability in electronic packaging, Microelectron. Reliab. 42 (4–5) (2002) 607–627.
[82] S. Lavenstein, Y. Gu, D. Madisetti, J.A. El-Awady, The heterogeneity of persistent slip band nucleation and evolution in metals at the micrometer scale, Science 370 (6513) (2020) eabb2690.
[83] Y. Cui, G. Po, N. Ghoniem, Suppression of localized plastic flow in irradiated materials, Scr. Mater. 154 (2018) 34–39.
[84] T. Bieler, P. Eisenlohr, F. Roters, D. Kumar, D. Mason, M. Crimp, D. Raabe, The role of heterogeneous deformation on damage nucleation at grain boundaries in single phase metals, Int. J. Plast. 25 (9) (2009) 1655–1683.
[85] H. Wu, S. Huang, H. Zhu, Z. Xie, Strengthening FeCrNiCu high entropy alloys via combining v additions with in-situ TiC particles, Scr. Mater. 195 (2021) 113724.
[86] H. Wu, M. Huang, Q. Li, J. Wu, J. Li, Z. Wang, G. Fan, Manipulating the plastic strain delocalization through ultra-thinned hierarchical design for strength-ductility synergy, Scr. Mater. 172 (2019) 165–170.

[87] A. Hua, J. Zhao, Shear direction induced transition mechanism from grain boundary migration to sliding in a cylindrical copper bicrystal, Int. J. Plast. 156 (2022) 103370.
[88] S.K. Bhogaraju, H. R. Kotadia, F. Conti, A. Mauser, T. Rubenbauer, R. Bruetting, M. Schneider-Ramelow, G. Elger, Die-attach bonding with etched micro brass metal pigment flakes for high-power electronics packaging, ACS Appl. Electron. Mater. 3 (10) (2021) 4587–4603.
[89] A.D. Albert, M.F. Becker, J.W. Keto, D. Kovar, Low temperature, pressure-assisted sintering of nanoparticulate silver films, Acta Mater. 56 (8) (2008) 1820–1829.
[90] Z. Zhang, D. Lunt, H. Abdolvand, A.J. Wilkinson, M. Preuss, F.P. Dunne, Quantitative investigation of micro slip and localization in polycrystalline materials under uniaxial tension, Int. J. Plast. 108 (2018) 88–106.
[91] L. Zou, C. Yang, Y. Lei, D. Zakharov, J.M. Wiezorek, D. Su, Q. Yin, J. Li, Z. Liu, E.A. Stach, et al., Dislocation nucleation facilitated by atomic segregation, Nat. Mater. 17 (1) (2018) 56–63.
[92] M. Thieme, K.-P. Wieters, F. Bergner, D. Scharnweber, H. Worch, J. Ndop, T. Kim, W. Grill, Titanium powder sintering for preparation of a porous functionally graded material destined for orthopaedic implants, J. Mater. Sci., Mater. Med. 12 (2001) 225–231.